Controls on fault zone structure and brittle fracturing in the foliated hanging-wall of the Alpine Fault

Jack N. Williams[a]*, Virginia G. Toy[a], Cécile Massiot[b,c], David D. McNamara[c,d], Steven A. F. Smith[a], Steven Mills[e]

Affiliations:

[a]Department of Geology, University of Otago, PO Box 56, Dunedin 9054, New Zealand

[b]School of Geography, Environment, and Earth Sciences, Victoria University of Wellington, PO Box 600, Wellington 6012, New Zealand

[c]GNS Science, PO Box 30-368, Lower Hutt 5040, New Zealand

[d]Department of Earth and Ocean Sciences, NUI Galway, University Road, Galway, Ireland

[e]Department of Computer Science, University of Otago, PO Box 56, Dunedin 9054, New Zealand

***Corresponding Author:** Jack Williams, now at: School of Earth and Ocean Sciences, Cardiff University, Cardiff, CF10 3AT, United Kingdom (email: williamsj132@cardiff.ac.uk)

Abstract

Three datasets are used to quantify fracture density, orientation, and fill in the foliated hanging-wall of the Alpine Fault: (1) X-ray computed tomography (CT) images of drill-core collected within 25 m of its principal slip zones (PSZs) during the first phase of the Deep Fault Drilling Project that were reoriented with respect to borehole televiewer images, (2) field measurements from creek sections up to 500 m from the PSZs, and (3) CT images of oriented drill-core collected during the Amethyst Hydro Project at distances of ~0.7-2 km from the PSZs. Results show that within 160 m of the PSZs in foliated cataclasites and

25 ultramylonites, gouge-filled fractures exhibit a wide range of orientations. At these distances,

26 fractures are interpreted to have formed at relatively high confining pressures and/or in rocks

27 that had a weak mechanical anisotropy. Conversely, at distances greater than 160 m from the

28 PSZs, fractures are typically open and subparallel to the mylonitic or schistose foliation,

29 implying that fracturing occurred at low confining pressures and/or in rocks that were

30 mechanically anisotropic. Fracture density is similar across the ~500 m width of the field

31 transects. By combining our datasets with measurements of permeability and seismic velocity

32 around the Alpine Fault, we further develop the hierarchical model for hanging-wall damage

33 structure that was proposed by Townend et al., (2017). The wider zone of foliation-parallel

34 fractures represents an 'outer damage zone' that forms in the near-surface. The distinct <160

35 m wide interval of widely oriented gouge-filled fractures constitutes an 'inner damage zone.'

36 This zone is interpreted to extend towards the base of the seismogenic crust given that its

37 width is comparable to: (1) the Alpine Fault low-velocity zone detected by fault zone guided

38 waves, and (2) damage zones reported from other exhumed large-displacement faults. In

39 summary, a narrow zone of fracturing at the base of the Alpine Fault's hanging-wall

40 seismogenic crust is anticipated to widen in the near-surface, which is consistent with fault

41 zone flower structure models.

42 **Keywords**: fractures, anisotropy, Alpine Fault, Deep Fault Drilling Project, damage zone

43 **1. Introduction**

44 Conceptual models of fault zone structure in the upper crust often invoke a relatively narrow

45 "fault core" that accommodates most displacement, surrounded by a halo of heavily fractured

46 rock termed the "damage zone" (Caine et al., 1996; Chester et al., 1993; Chester and Logan,

47 1986; Faulkner et al., 2010). These models have been successfully applied in a variety of

48 tectonic settings and for a wide range of fault displacements and exhumation depths (e.g.

49 Choi et al., 2016; Faulkner et al., 2010; Kim et al., 2004; Mitchell and Faulkner, 2009;

50 Savage and Brodsky, 2011). However, the term "damage zone" has been applied by

51 geologists and geophysicists to describe a variety of fault-related features, such as fractures

52 and faults at stepovers and bends (Chester and Chester, 2000; Kim et al., 2004; Mitchell and

53 Faulkner, 2009; Wilson et al., 2003), the volume of inelastic deformation that is induced by

54 dynamic stresses during earthquake rupture propagation (Andrews, 2005; Cowie and Scholz,

55 1992; Rice et al., 2005; Templeton et al., 2008; Vermilye and Scholz, 1998), and the volume

56 of rock in which earthquake swarms or foreshock and aftershock sequences are localised

57 (Kim and Sanderson, 2008; Savage et al., 2017; Sibson, 1989; Yukutake et al., 2011).

58 Furthermore, though damage zones are typically reported to be <1 km wide (Faulkner et al.,

59 2011; Savage and Brodsky, 2011), co-seismic ground shaking can modify fracture

60 permeability many hundreds of kilometres away from the fault source (Cox et al., 2015;

61 Muir-Wood and King, 1993; O'Brien et al., 2016).

62

63 Brittle faults often develop in mylonite sequences or other (e.g. jointed) rocks that contain

64 compositional and mechanical anisotropies (Bistacchi et al., 2012; Chester and Fletcher,

65 1997; Massironi et al., 2011). Evidence from field studies (Bistacchi et al., 2010; Peacock and

66 Sanderson, 1992), experiments (Donath, 1961; Misra et al., 2015; Paterson and Wong, 2005),

67 and numerical modelling (Chester and Fletcher, 1997) demonstrates that such anisotropy can

68 significantly affect the orientation and density of brittle fractures. Despite this, "fault core-

69 damage zone" models are based largely on field observations from relatively isotropic host

70 rocks, and there have been comparatively few field studies (a notable exception being,

71 Bistacchi et al., (2010)) that document the influence of mechanical anisotropy on patterns of

72 brittle fracture damage in large-displacement faults.

73

74 In this contribution, multiple datasets across a range of scales were used to analyse fracture

75 densities, orientations, and mineral fills across the hanging-wall of the Alpine Fault's central

76 section. Measurements from within 25 m of the Alpine Fault principal slip zones (PSZs) were

77 made from shallow (depths <130 m) drill-cores and wireline logs obtained during the first

78   phase of the Deep Fault Drilling Project (DFDP-1). These are combined with field studies at

79   distances <500 m from the PSZs and analyses of drill-core recovered at 0.7-2 km from the

80   PSZs during the Amethyst Hydro Project (AHP). Results are then compared to measurements

81   of hydraulic conductivity (Cox et al., 2015; Townend et al., 2017) and geophysical studies

82   (Boese et al., 2012; Chamberlain et al., 2017; Eccles et al., 2015) around the Alpine Fault. In

83   doing so, we critically assess the application of "damage zone" models to a plate-boundary-

84   scale structure. Furthermore, the Alpine Fault is an active fault that rapidly exhumes ductile-

85   to-brittle fault rock sequences from depths of up to 35 km (Little et al., 2005; Norris and Toy,

86   2014). Fracturing in its hanging-wall therefore overprints a 1-2 km wide mylonite sequence

87   containing a pervasive foliation (Cooper and Norris, 1994; Norris and Cooper, 1997, 2007;

88   Toy, 2008), and so can provide new insights into the relationships between fracturing and

89   mechanical anisotropy.

90

2. Tectonic setting of the Alpine Fault

92   The Alpine Fault is a crustal-scale (along strike extent ~850 km, depth ~35 km) transpressive

93   discontinuity accommodating ~70% of Pacific-Australian plate motion in the South Island of

94   New Zealand (DeMets et al., 1994; Norris and Cooper, 2001, Figure 1a). This study focuses

95   on the central section between the Toharoa and Martyr Rivers (Barth et al., 2013) where it

96   currently accommodates dextral strike-slip at a rate of 27 ± 5 mm/yr and dip-slip at a rate of

97   6-10 mm/yr (Little et al., 2005; Norris and Cooper, 2001).

98

99   In the central section at depths greater than 8-12 km, the Alpine Fault accommodates motion

100   via viscous creep across a >1 km wide ductile shear zone in which the hanging-wall "Alpine

101   Schist" protolith is progressively mylonitised (Norris and Cooper, 2007; Toy et al., 2010).

102   Shear strains increase with proximity to the Alpine Fault and are recorded by protomylonites,

103   mylonites and ultramylonites, which occur in spatial sequence towards the fault (Figure 2;

104   Norris and Cooper, 2003; Reed, 1964; Toy et al., 2008). Foliation in the mylonite sequence is

105   mainly defined by alternating quartzofeldspathic and mica-rich layers (Figure 2). Bottle-green

106   hornblende-rich metabasic mylonites, and purple-dark grey mylonites that are comparatively

107   mica rich are also present. Their presence reflects variations in protolith lithology (Cooper

108   and Norris, 2011; Norris and Cooper, 2007; Sibson et al., 1981; Toy, 2008). As the mylonites

109   in the hanging-wall are exhumed to depths of less than 8-12 km, temperatures drop below

110   those at which quartz plasticity occurs and brittle structures start to overprint the mylonitic

111   shear zone (Norris and Cooper, 2007; Toy et al., 2010, 2015). This brittle overprint is

112   reflected in the formation of a ~20 m thick layer of green, indurated and often foliated

113   cataclasite (Allen et al., 2017; Toy et al., 2015), and a 10-50 cm thick clay-rich PSZ that is

114   preserved adjacent to the currently-active fault trace (Boulton et al., 2017, 2012; Ikari et al.,

115   2014; Mitchell and Toy, 2014).

116

117   To the first-order (i.e. at scales >10 km), the trace of the Alpine Fault is remarkably linear,

118   with an average strike of 055º (Norris and Cooper, 2007). On the basis of geophysical

119   imaging and measurements of the mylonitic foliation -which is thought to parallel the fault- it

120   is estimated to dip at ~45º in its central section (Sibson et al., 1981; Stern et al., 2007), though

121   this may locally exceed 60º (Little et al., 2005; Toy et al., 2017). At scales of 1-10 km,

122   perturbations in the regional stress field induced by hanging-wall topography results in

123   segmentation of the Alpine Fault. Segmentation is rooted to depths of 0.5-4 km and comprises

124   km-long, approximately E-W striking and steeply-dipping strike-slip fault strands, which

125   adjoin NE-SW striking, gently-dipping (~30º) thrust segments (Barth et al., 2012; Langridge

126   et al., 2014; Norris and Cooper, 1995, 2007; Simpson et al., 1994; Upton et al., 2017).

3. Methods

3.1 Fracture orientations from DFDP-1 drill-core

Hanging-wall fracture orientations immediately adjacent to the Alpine Fault's PSZ were assessed through analysis of datasets arising from the first phase of the Deep Fault Drilling Project (DFDP-1, http://alpine.icdp-online.org). DFDP-1 successfully sampled the Alpine Fault in two boreholes (DFDP-1A and DFDP-1B, Figure 3) at depths of less than 150 m at Gaunt Creek (Figure 1b, Sutherland et al., 2012). The geophysical properties of the DFDP-1 boreholes were characterised by a full suite of wireline logs (Townend et al., 2013). These were combined with visual descriptions of ~70 m of core recovered across the two boreholes to construct a lithological classification scheme for DFDP-1 drill-core (Figure 3, Toy et al., 2015).

Abundant fractures were observed in X-ray computed tomography (CT) scans of DFDP-1 drill-core (Williams et al., 2016). The true orientations of these fracture were obtained by generating 'unrolled' CT images of individual core sections (Mills and Williams, 2017), which are directly analogous to geographically referenced - but lower resolution - borehole televiewer (BHTV) images. Where fractures could be matched between the two images, a rotation could be derived to transform all fracture orientations in the CT scans from a local core reference frame to their true geographic orientation (Figure 4). Depending on the number of fractures matched, core was rotated with a high, moderate, or low degree of confidence. In DFDP-1A, the quality of BHTV imaging was insufficient to attempt matching fractures, whereas in the Alpine Fault's relatively intact footwall (Townend et al., 2013), too few fractures (<1 fracture/core-section) could be imaged to attempt core reorientation. Therefore, the true orientation of fractures was only determined for the depth interval 94-126 m in the DFDP-1B borehole (Figure 3). Given the orientation of the PSZ-1 (which separates hanging-wall and footwall cataclasite) sampled in DFDP-1 (015/43 E; Townend et al., 2013), this

153   spans an orthogonal distance of ~25 m. A full methodology is provided in Appendix A, the

154   rotations applied to DFDP-1 core sections are listed in Table S1, and a complete CT-BHTV

155   image comparison is given in Williams et al. (2017b).

156

157   3.2 Field observations of fracture orientations and densities

158   At orthogonal distances of up to 150-250 m from the PSZs, fracture orientations and densities

159   were measured in four creeks (Gaunt Creek, Stony Creek, Hare Mare Creek and Havelock

160   Creek, Figure 1b) that cut across the hanging-wall sequence approximately perpendicular to

161   the main fault trace (Figure S1). Along each creek, fracture orientations and densities were

162   measured at 3 or 4 stations. This information was also gathered from approximately 500 m

163   from the Alpine Fault at Bullock Creek (Figure 1b). Each creek transect cuts across a thrust

164   segment of the Alpine Fault, so the orthogonal distance between the measuring stations and

165   the PSZs was calculated assuming a fault dip of 30º (Norris and Cooper, 1995, 1997). The

166   mylonite lithology for each station was classified using the scheme presented by Toy (2008).

167

168   The outcrops encountered along these transects are typically sub-vertical and may be covered

169   by debris except at their bases where they are frequently cleaned by flood events (Figure S2).

170   They are therefore poorly-suited for fracture density analysis using circular scanlines (e.g.

171   Mauldon et al., 2001). Instead, the fracture density was calculated from the number and

172   orientation of fractures that intersected a linear transect along the base of each outcrop (Priest,

173   1993; Schulz and Evans, 2000). This technique has the tendency to under-sample fractures

174   oriented at low angles to the scan-line. Therefore, a weighting (w) factor calculated using a

175   modified version of the Terzaghi correction (Massiot et al., 2015; Terzaghi, 1965) was

176   applied to each fracture, and results are shown as 'corrected' fracture density.

177

178   3.3 Fracture orientations in the Amethyst Hydro Project boreholes

179   The Amethyst Hydro Project (AHP) was developed to divert water from the Amethyst Ravine

180   down a 1040 m-long tunnel to a powerhouse on the floodplain of the Wanganui River. Prior

181   to the main phase of tunnelling, four exploratory boreholes (BH1-4; Figure 1b and S3) were

182   completed between 2005-2006, resulting in the recovery of ~890 m of drill-core at depths of

183   50-200 m. The boreholes are situated 1-2 km southeast of a thrust segment of the Alpine

184   Fault, where it may conceivably dip at a range of 30-60º (Norris and Cooper, 1995; Toy et al.,

185   2017). The drill-cores are therefore at orthogonal distances of ~0.7-2.0 km from the PSZs.

186

187   To provide a dataset analogous to the DFDP-1 CT scans, a total of 31.9 m of drill-core from

188   the AHP boreholes was CT scanned at the Southern Cross Hospital in Wellington, New

189   Zealand. Initial descriptions of the drill-core found that the Rock Quality Designation (RQD,

190   the % of intact core lengths >100 mm/1 m of drill-core) varied considerably due to intense

191   fracturing adjacent to the Tarpot Fault and other minor faults that intersect the AHP boreholes

192   (Geotech Consulting Limited, 2006; Savage, 2013). However, for practical reasons scanning

193   was focussed on intervals of high RQD (Figure S3). The CT scanner was operated at 100 mA

194   and an X-ray tube voltage of 120 kVp. Slice spacing was 1.25 mm, field of view 250 mm, and

195   the image size was 512 x 512 pixels. Therefore, the size of one voxel is 0.488 x 0.488 x 1.25

196   mm in the x, y, z directions respectively. Reconstruction of two-dimensional CT slices into

197   three-dimensional images of the drill-core was performed using OsiriX Imaging Software

198   (http://www.osirix-viewer.com/).

199

200   AHP drill-core was not oriented. However, the orientation of the schistosity is noted in the

201   drill-core logs to an accuracy of ±5° (Geotech Consulting Limited, 2006), where it is

202   consistent with the schistosity orientation measured in the Amethyst Tunnel itself (Savage,

203   2013). It can thus be used as a reference to reorient drill-core CT scans back into a geographic

204 reference frame. For BH2 and BH3 drill-cores, which are vertical, this required only a single

205 transformation. For the inclined BH1 and BH4 drill-cores, this required first rotating the core

206 with respect to the foliation. These orientations were then corrected for the inclination of the

207 drill core using the Planes from Oriented and Navigated Drillcore (POND) Excel spreadsheet

208 (Stanley and Hooper, 2003).

209 3.4 Statistical analysis of fracture orientations

210 The clustering intensity of fracture orientations was quantified using the resultant vector

211 method of Priest, (1993), where the vector for each fracture was weighted by the Terzaghi

212 correction for misorientation bias (Massiot et al., 2015; Terzaghi, 1965). This analysis was

213 performed only for the DFDP-1 and AHP datasets, which sampled a large population (>100)

214 of fractures. Field measuring stations sampled too few (<30) fractures to reliably perform this

215 analysis, and so their clustering is described in a qualitative sense only.

216 **4. Results**

217 4.1 Fracture orientations in DFDP-1 drill-core within 25 m of the Alpine Fault

218 In the DFDP-1 CT images, a total of 637 fractures were rotated into their true geographic

219 orientation where they show a weak cluster about the orientation of the foliation and Alpine

220 Fault PSZs at Gaunt Creek (015/43 E, Figures 5a, Appendix B; Townend et al., 2013).

221 Features in DFDP-1B BHTV images are also aligned about this orientation, but with a higher

222 cluster intensity than fractures noted in the CT images (Figure 5b, Table 1). This may reflect:

223 (1) features observed at the resolution of the BHTV are more likely to be aligned subparallel

224 to the fault plane and foliation than those visible in CT, and/or (2) some of the planar features

225 identified from the BHTV images were the mylonitic foliation itself. The clustering of

226 fractures hosted in foliated ultramylonites and cataclasites (Units 1, 2 and 4 of Toy et al.,

227 2015) is the same as fractures hosted in relatively homogenous unfoliated cataclasites (Unit 3

228 of Toy et al., 2015; Figures 5c and d, Table 1). We also observed no clear relationships

229 between fracture fill (Table 1 of Williams et al., 2016) and fracture orientation (Figure 5a).

230

231 4.2 Fracture orientations, densities, and fill in field transects within 500 m of the Alpine Fault

232 The orientations and densities of fractures observed in the four field transects are summarised

233 in Figure 7. In these transects, similar fractures to those observed in the CT scans of DFDP-1

234 core are identified (Figure 8). Total fracture density in the transects varies between 3-30

235 fractures/metre, and there is no clear decrease in fracture density with increasing distance

236 from the Alpine Fault in any of the transects (Figure 7a). Gouge-filled fractures (Figure 8a-c)

237 are observed at all distances from the Alpine Fault but are relatively abundant (>1

238 fracture/metre, Figure 7a, Table S2) within 100-160 m of the PSZs (Figure 7a). The thicker

239 gouge-filled fractures (>1 cm) commonly juxtapose different lithologies or offset markers

240 (Figure 8d-f). Thinner gouge-filled fractures (<1 cm) are localised within 160 m of the Alpine

241 Fault. Open fractures (Figure 8g-i) are present at all stations, though are most prevalent at

242 those furthest from the fault (Figure 7b).

243

244 The composition of the mylonites can also affect fracture density. When they are juxtaposed

245 together, micaceous mylonites and ultramylonites are observed to contain relatively high

246 densities of gouge-filled fractures compared to quartzofeldspathic mylonites and

247 ultramylonites (Figures 9). Localities that showed the widest range in fracture orientations

248 tend to be less than 160 m from the PSZs within the ultramylonites (Figure 7b). Within

249 mylonite units, fracture orientations tend to be more aligned to the foliation (Figure 7b),

250 although gouge-filled fractures can sometimes cut across it (e.g. Bullock Creek).

251

252 4.3 Fractures in AHP drill-core, 0.7-2.0 km from the Alpine Fault

253 The AHP sampled grey, well-foliated Alpine Schist (Figure 10), a subgroup of the Haast

254 Schist (textural zone III-IV, Turnbull et al., (2001); Cox and Barrell., (2007)). Fracture

255 orientations are clustered about the orientation of the host rock schistosity in agreement with

256 the findings during initial drill-core descriptions and observations within the Amethyst

257 Tunnel itself (Figure 11; Geotech Consulting Limited, 2006; Savage, 2013). The clustering of

258 these fracture orientations is stronger than in the DFDP-1 datasets (Table 1). Fractures that

259 cut across the schistosity are most frequent in BH4 (Figure 10d and 11).

260

261 Though fractures are predominantly open, it is conceivable that the original fill may have

262 been lost during the subsequent core handling processes. This means that standard schemes to

263 differentiate between natural and induced fractures (Kulander et al., 1990; Williams et al.,

264 2016) cannot be applied to this dataset. Nevertheless, some open fractures must be natural as

265 they show alteration haloes (Figure 10a) implying that they were once conduits for fluid-flow.

266 Furthermore, packer tests conducted in these boreholes indicate hydraulic conductivities of

267 $\sim 10^{-6}$-10^{-5} ms^{-1}, which is equivalent to permeabilities of 10^{-13}-10^{-12} m^2 (Cox et al., 2015;

268 Geotech Consulting Limited, 2006). No permeability measurements have been made in the

269 schist protolith at greater distances from Alpine Fault, however, these measurements are

270 orders of magnitude higher than has been reported in other metamorphic rock terranes ($\sim 10^{-20}$-10^{-17} m^2; Manning and Ingebritsen, 1999) and for typical continental crust ($\sim 10^{-17}$ m^2;

272 Townend and Zoback, 2000).

273 **5 Discussion**

274 5.1 Fracture orientations in anisotropic wall rocks in the Alpine Fault hanging-wall

275 Two styles of fracturing are evident in the foliated Alpine Fault cataclasite, mylonite and

276 schist sequence (Figure 12). Within DFDP-1 drill-core, fractures are predominantly gouge-

277   filled and exhibit a range of orientations (Figure 5 and 6) with only a small proportion (11%)

278   of fractures in foliated cataclasites and ultramylonites clearly foliation-parallel (Williams et

279   al., 2016). However, in schists sampled by the AHP drill-core, the fractures are more

280   clustered about the foliation than in DFDP-1 drill-core (Figure 11, Table 1). The difference in

281   fracture clustering between the DFDP-1 and AHP drill-cores is qualitatively replicated by the

282   field transects, where fractures show variable orientations immediately adjacent to the Alpine

283   Fault but are typically foliation-parallel at the sites furthest from the fault (Figure 7).

284   Furthermore, field transects show that the variably oriented fractures have a gouge-fill, whilst

285   foliation-parallel fractures further from the fault tend to be open (Figures 7 and 8).

286

287   Experimental studies on foliated rocks demonstrate that mechanical anisotropy will exert the

288   greatest control on rock failure when: (1) the angle between the maximum principal stress

289   (σ_1) and the anisotropy (α) is ~30º, (2) confining pressure is low (<35 MPa), and (3) the

290   mechanical 'strength' of the anisotropy is high (Donath, 1961; Misra et al., 2015; Nasseri et

291   al., 2003; Paterson and Wong, 2005). The first factor can be approximated for the Alpine

292   Fault given the mylonite's average orientation of 055/45SE (Norris and Cooper, 2007) and

293   the stress tensor orientation within the surrounding crust, determined from focal mechanisms

294   of microseismicity in the fault's hanging-wall (Boese et al., 2012). This yields a value of α of

295   approximately 44º, when measured in the plane containing the maximum and minimum

296   principal stresses. This can be considered an intermediate value of α, since in deformation

297   experiments fractures may form parallel or non-parallel to the foliation depending on the

298   combination of confining pressure and lithology (Donath, 1961; Nasseri et al., 2003; Paterson

299   and Wong, 2005).

300

301   Foliation-parallel fractures are least common in the ultramylonites and foliated cataclasites.

302   Indeed, in the DFDP-1 datasets, there is no difference in fracture clustering between foliated

303   and unfoliated units (Table 1). Lithology may control mechanical anisotropy depending on

304   mineralogy, porosity, grain size, and the nature of the foliation surfaces (Donath, 1961;

305   Nasseri et al., 2003). It is notable that phase mixing and grain size reduction in the

306   ultramylonites reduces the intensity of the foliation, compared to the relatively coarse-grained

307   schists, protomylonites, and mylonites (Figure 2; Norris and Cooper, 2007; Toy et al., 2010,

308   2008). These data suggest that this lithological change could have a marked effect on the

309   orientation of fractures. Compositional variations between relatively quartzofeldspathic and

310   relatively micaceous mylonites can also influence the density of fractures (Figure 9). These

311   observations highlight that fracturing in the upper crust may be influenced by lithological

312   variations developed within an underlying linked, and synkinematic, shear zone. However, at

313   other localities (e.g. Stony Creek, Figure 7), variations in dominant fracture characteristics are

314   confined within units of similar composition and texture. This suggests that variations in

315   confining pressure may also be important in controlling the relationship between fractures and

316   foliation, as discussed in the next section.

317

318   5.2 Fracture damage around the Alpine Fault

319   Field transects across the Alpine Fault's hanging-wall show that fracture density remains

320   roughly constant (>3.5 fractures/m, corrected for orientation bias) for at least 500 m from the

321   fault (Figure 7a). Furthermore, the AHP (Cox et al., 2015) and DFDP-2B boreholes

322   (Sutherland et al., 2017; Townend et al., 2017) demonstrate an interval of enhanced

323   permeability (10^{-16}-10^{-13} m^2) that extends for at least 2 km into the Alpine Fault's hanging-

324   wall. Permeability in this rock mass is controlled by open fractures (Cox et al., 2015;

325   Sutherland et al., 2017; Townend et al., 2017) that are generally foliation-parallel (Massiot,

326   2017), and so directly analogous to the fractures sampled in the field (Figure 8g-i) and in

327   AHP drill-core (Figure 10). Conventional definitions of fault structure, that use fracture

328   density and permeability as criteria for damage zone width (e.g. Berg and Skar, 2005; Caine

329   et al., 1996; Faulkner et al., 2010; Savage and Brodsky, 2011; Schulz and Evans, 2000),

330   would therefore suggest that the Alpine Fault's damage zone extends for at least 500 m, and

331   possibly 2 km, into its hanging-wall.

332

333   Nevertheless, within the field transects we also note a distinct interval adjacent to the Alpine

334   Fault's PSZs that contains a relatively high density of gouge-filled fractures (>1

335   fracture/metre, Figure 7a). The width of this interval is <147 m (i.e. station 4) from the PSZs

336   at Gaunt Creek, <103 m at Stony Creek (i.e. station 3), <151 m at Hare Mare Creek (at station

337   2, Figure 8c) and <160 m at Havelock Creek (i.e. stations 4). These width estimates are based

338   on assumption that the Alpine Fault dips at 30° below the measuring stations (see the methods

339   section). However, the fault dip may locally vary (for example, the fault dip sampled by

340   DFDP-1 was 43°; Townend et al., (2013)), and there is also uncertainty in the depth extent of

341   its near-surface segmentation (Barth et al., 2012; Norris and Cooper, 1995; Upton et al.,

342   2017). Nevertheless, even if the fault dipped at 45° (Norris and Cooper, 2007) beneath the

343   measuring stations, the zone of higher-density gouge-filled fractures would be <205 m wide

344   (Table S3) and so is still appreciably closer to the Alpine Fault than the intervals sampled by

345   the AHP and DFDP-2 boreholes.

346

347   It is this ~100-160 m wide interval with a high density of gouge-filled fractures that Norris

348   and Cooper (1997, 2007) interpreted as the extent Alpine Fault's central section hanging-wall

349   damage zone. Furthermore, the width of this zone is comparable to damage zones widths

350   estimated elsewhere on the Alpine Fault (e.g. Barth et al., 2013 along the southern section;

351   Wright, 1998 at the northern end of the the central section, Figure 13a) and to other crustal-

352   scale fault zones that have accommodated hundreds of kilometres of displacement (Figure

353   13b; Faulkner et al., 2011; Savage and Brodsky, 2011).

354

355   Interpretations of damage zone width within the Alpine Fault's hanging-wall may therefore

356   differ by an order of magnitude depending on what criteria is used. To reconcile this,

357   Townend et al., (2017) suggested that the ~2 km wide interval of enhanced permeability and

358   foliation-parallel fracturing can be considered as an 'outer damage zone' (Figure 12).

359   Fractures within this zone may have formed by co-seismic shaking and slip on critically-

360   stressed fractures (Cox et al., 2015; Townend et al., 2017), or by the release of confining

361   pressure (Engelder, 1985; Price, 1959; Zangerl et al., 2006) during rapid exhumation (6-9

362   mm/yr) of the hanging-wall (Little et al., 2005; Tippett and Kamp, 1995). Rare gouge-filled

363   fractures (<1 fracture/metre) in this interval (e.g. Figure 8e) may also be the structures

364   accommodating the diffuse, low to moderate magnitude (M_W <6) seismicity that has been

365   recorded in a ~5 km wide zone within the Alpine Fault's hanging-wall (Boese et al., 2012;

366   Chamberlain et al., 2017; Eberhart-Phillips, 1995).

367

368   Conversely, the <160 m wide zone with a relatively high density of gouge-filled fractures

369   defines a narrower 'inner damage zone' (Figure 12; Townend et al. 2017). Microstructural

370   and compositional analysis of these fractures indicates that they formed in response to wear

371   and shearing of the wall rock and were subsequently mineralised due to circulation of

372   hydrothermal fluids (Warr and Cox, 2001; Williams et al., 2017a). Offset markers across

373   gouge-filled fractures (particularly those <1 cm thick) are rarely observed in DFDP-1 core

374   and field transects, but where they are present, reverse offset is most frequently noted (Figure

375   8d; Norris and Cooper, 1997; Toy et al., 2015). "Gouge-filled shears" that accommodated

376   strike-slip (Norris and Cooper, 1997), normal dip-slip (Cooper and Norris, 1994), or a

377   combination of both (Barth et al., 2012) have also been observed.

378

379   Cooper and Norris, (1994) interpreted that dip-slip fractures facilitated imbrication, tectonic

380   thickening and rotation of Alpine Fault thrust sheets as they moved across the irregular

381   topography of the footwall gravels. Dextral shears are interpreted to reflect the partitioning of

382   strike-slip movement away from shallowly dipping PSZs (Barth et al., 2012). The diverse

383   range of fracture orientations and shear senses in gouge-filled fractures therefore indicates

384   complex internal deformation of Alpine Fault thrust sheets in the near-surface (<500 m), as

385   they facilitate transpressional motion under the influence of km scale along-strike variations

386   in stress induced by the topography (Norris and Cooper, 1995; Upton et al., 2017).

387

388   Fractures may have also formed due to dynamic off-fault stresses (Ma, 2009; Rice et al.,

389   2005) during M_W >7.5 Alpine Fault earthquake ruptures (Sutherland et al., 2007). The

390   relatively thin seismogenic crust in the Alpine Fault's hanging-wall (10 ± 2 km, Boese et al.,

391   (2012)) will limit the generation of dynamic co-seismic damage to within ~100-200 m of the

392   fault (Ampuero and Mao, 2017). To the first order, this is comparable to the width of the

393   inner damage zone reported here.

394

395   5.3 Comparison to geophysical data

396   A 60-200 m wide low-velocity zone (LVZ) that extends to depths of ~8 km has been

397   documented around the Alpine Fault from the detection and character of Fault Zone Guided

398   Waves (FZGWs; Eccles et al., 2015). FZGWs are commonly regarded as an *in situ* indicator

399   of fault damage zone width (Ben-Zion and Sammis, 2003; Eberhart-Phillips et al., 1995;

400   Ellsworth and Malin, 2011; Li et al., 2014). Given the comparable widths of the Alpine Fault

401   LVZ (60-200 m) and the inner damage zone described here (100-160 m), we speculate that

402   the inner damage zone may trap FZGWs in the Alpine Fault hanging-wall. If this is true, it

403   implies that the inner damage zone extends to depths of ~8 km, consistent with the relatively

404   high-temperature (<400 °C) mineralising phases (calcite and chlorite) present in the gouge-

405   filled fractures (Williams et al., 2017a).

406

407 Though the boundary between the mylonites and ultramylonites is also ~100 m from the

408 Alpine Fault (Norris and Cooper, 2003; Toy et al., 2008), these two units have roughly

409 similar seismic velocities (Adam et al., 2016; Allen et al., 2017; Christensen and Okaya,

410 2007) and so are unlikely to channel FZGWs. We also note that since FZGWs are an

411 indicator of total fault zone width, our interpretation implies that most of the Alpine Fault's

412 LVZ is located in its hanging-wall. Western Province basement rocks to the west of the

413 Alpine Fault are rarely exposed (Lund Snee et al., 2014; Norris and Cooper, 2007), and so it

414 remains unknown if its footwall damage zone is indeed relatively narrow.

415 .

416 That the FZGWs are not being channelled by the margins of the ~2 km wide outer damage

417 zone leads us to conclude that this is a near-surface feature only (i.e. fractures are not kept

418 open at depth by pressurised fluids). If correct, this model of the Alpine Fault's hanging-wall

419 structure conforms to the expectations of fault zone flower structure models, which predict a

420 narrow inner damage zone that extends through the seismogenic crust, surrounded by a wider

421 zone of fractures in the near-surface at low confining pressures (~<3 km, Figure 12; e.g. Finzi

422 et al., 2009; Sylvester, 1988).

423

424 **6. Conclusions**

425 Fracture orientations and densities in the foliated hanging-wall of the Alpine Fault's central

426 section were quantified in drill-core from the Deep Fault Drilling Project (DFDP-1), field

427 transects in four creek sections, and drill-core recovered from the Amethyst Hydro Project. At

428 distances greater than approximately 160 m from the Alpine Fault principal slip zones (PSZs),

429 open and foliation-parallel fractures dominate. These are interpreted to form at low confining

430 pressures in mechanically anisotropic schist and mylonites. At distances less than ~160 m

431 from the PSZs, gouge-filled fractures with a wide range of orientations predominate. Fracture

432 density and orientation are locally influenced by changes in host rock lithology, but overall

433 fracture density is approximately constant at distances of up to ~500 m from the PSZs (Figure

434 12).

435

436 Following Townend et al., (2017), we interpret that the ~2 km wide zone of open foliation-

437 parallel fractures within the hanging-wall represents an "outer damage zone" that forms at

438 low confining pressures and relatively shallow depths. Conversely, the 160 m-wide zone of

439 gouge-filled fractures represents an "inner damage zone." The width of this zone is similar to

440 estimates for the low-velocity zone (LVZ) around the Alpine Fault made by Fault Zone

441 Guided Waves. We therefore interpret that the inner damage zone is the geological

442 manifestation of the LVZ, which if true, implies that the inner damage zone also extends to

443 depths of ~8 km. Overall, our interpretations are compatible with a flower structure model for

444 damage in the Alpine Fault's hanging-wall, with a relatively narrow zone of damage

445 extending towards the base of the seismogenic crust, which broadens upwards towards the

446 surface.

447 **Code availability**

448 The code to generate 'unrolled' circumferential CT images is available from the GFZ data

449 service (http://pmd.gfz-

450 potsdam.de/panmetaworks/review/7f1b114f11b67f540bb1360ead692dc578a66e3d0935c7fef

451 6ffe210db285300-icdp/).

452 **Data availability**

453 In the supplementary information, we include detailed field maps and cross sections (Figure

454 S1), photos of outcrops used for quantifying fracture density (Figure S2), a cross section

455 through the Amethyst Tunnel and location of boreholes (Figure S3), and an example of AHP

456 CT scans (Figure S4). The following tables are also provided, a list of rotations applied to

457 DFDP-1B core (Table S1), a summary of field transects (Table S2), and estimates of the

458   distance of field measuring stations from the Alpine Fault for different fault dips (Table S3).

459   Lithological distribution and Alpine Fault location as per University of Otago fault zone

460   mapping program, which is available at: http://www.otago.ac.nz/geology/research/structural-

461   geology/alpine-fault/af-maps.html. DFDP-1 and AHP CT scan 'core logs' and CT-BHTV

462   image comparison are available on the GFZ data service (http://pmd.gfz-

463   potsdam.de/panmetaworks/review/52b75045a30f1bd60f7fd5b841e69c468885e2a10dfc3704e

464   50b236df2ef8608-icdp).

465

Acknowledgements

467   DFDP-1 was funded by: GNS Science; Victoria University of Wellington; the University of

468   Otago; the University of Auckland; the University of Canterbury; Deutsche

469   Forschungsgemeinschaft and the University of Bremen; Natural Environment Research

470   Council grants NE/J024449/1, NE/ G524160/1 and NE/H012486/1 and the University of

471   Liverpool; and the Marsden Fund of the Royal Society of New Zealand. The International

472   Continental Scientific Drilling Program, ICDP (www.icdp-online.org) provided extensive

473   support. JW was supported by a University of Otago Doctoral Scholarship. We thank

474   Matthew Parris at the Oncology Department at Dunedin Hospital, and Darren Tod at the

475   Southern Cross Hospital, Wellington, for support in collecting CT scans of DFDP-1 Amethyst

476   Hydro Project drill-core respectively. Katrina Sauer, Ben Melosh and Astrid Vetrhus

477   provided field assistance. Comments by Tim Little and Tom Blenkinsop, and by two

478   anonymous reviewers on an earlier version of this manuscript, improved this paper.

Appendix A: DFDP-1B core rotation methodology

480   The technique employed to reorient core DFDP-1 here is similar to that described in Jarrard et

481   al., (2001), Paulsen et al., (2002) and Shigematsu et al., (2014), however, instead of

482   comparing DFDP-1 BHTV data to DMT CoreScan system® unrolled core scans, we compare

483   BTHV images to 'unrolled' CT core images. The acquisition and interpretation of the DFDP-

484   1 BHTV logs has been previously described by Townend et al., (2013) and McNamara,

485   (2015). DFDP-1 CT scans consist of a stack of core-axial perpendicular image slices with a

486   pixel size of 0.244 mm and a spacing of 1 mm. The CT stack for each core section was loaded

487   into Fiji (http://fiji.sc/Fiji) and a circle was manually defined around the irregular boundary of

488   drill-core in a core axial-perpendicular image slice using the code available at Mills and

489   Williams, (2017). This circle was then used to define the path of the image in all other slices.

490   Generation of the unrolled images accounts for the fact that the spacing between individual

491   CT slices (1 mm, i.e. the core-axial parallel pixel size) is greater than the pixel size within the

492   slices (0.244 mm). Unrolled images were then reflected around the borehole axis as an image

493   of the outer surface of the core and a BHTV image are reflections of each other. This

494   technique has benefits over methods using the DMT CoreScan system®, since drill-core does

495   not have to be physically rotated and so can be used without the risk of damaging fragile core

496   sections.

497

498   Unrolled CT images were imported into the composite log viewing software WellCAD®

499   (http://www.alt.lu/wellcad.htm) along with the BHTV images, where they are placed side-by-

500   side to allow matching of structures (Figure 4, see also Williams et al., (2017b)). When

501   correlating the two datasets, it was first necessary to account for possible depth shifts between

502   recorded drill-core depths and BHTV imagery due to factors such as stretching of the logging

503   cable and intervals from which no drill-core was recovered (Haggas et al., 2001; Jarrard et al.,

504   2001). In this study, a depth shift of no more than ±30 cm was allowed.

505

506   The orientation of fractures in the DFDP-1 CT images had previously been measured within a

507   local core reference frame (see Figure 4 in Williams et al., 2016). Since the DFDP-1

508   boreholes were vertical, corrections to reorient the drill-core back into a geographic reference

509   frame required only a single rotation about the core axis to correct for the dip direction. When

510   correlating structures, errors may be introduced by: (1) the internal BHTV magnetometer

511   (±2°), (2) the manual picking of sinusoidal curves on BHTV and unrolled CT images that can

512   be ±10° for shallowly dipping (<30°) structures (Jarrard et al., 2001), and (3) the fact that the

513   DFDP-1B BHTV data imaged the open borehole, which has a larger diameter (127 mm) than

514   the drill-core (85 mm). To mitigate against the cumulative effect of these errors, Jarrard et al.,

515   (2001) stitched unrolled images of many different core sections together that spanned

516   intervals of 5-30 m, prior to the matching with BHTV imagery. This meant that only a single

517   rotation was necessary for all core sections across the entire stitched interval, which could be

518   based on identifying ~20-30 matching structures between the BHTV and unrolled core

519   images.

520

521   In DFDP-1 it was not possible to stitch unrolled CT images of core section together as no

522   prominent reference marker across different sections were identified. Consequently each <1

523   m long core section had to be reoriented individually, within which we never identified more

524   than 3 matching structures. Therefore, compared to the methodology described by Jarrard et

525   al., (2001), the degree of confidence on the applied reorientation was strongly dependent on

526   the quality of individual matches for each core section and the range of rotations that they

527   indicated. We recorded this qualitatively for each core section using the scheme outlined

528   below.

529

530   • High degree of confidence: images matched with one very prominent structure (e.g.

531   Figure 4d), or matched with two or more structures whose range of suggested

532   rotations are within 10° of each other (Figure 4b and c).

533

534   • Moderate degree of confidence: images matched with one prominent feature or two

535   features that indicate rotations that range 10-19° (e.g. Figure 4a) or three features

536   whose range of suggested rotations are within 20-30° of each other.

538 • Low degree of confidence: images matched with one feature or two features whose

539 range of suggested rotations are within 20-30° of each other.

540

541 In this scheme, a core reorientation is deemed unreliable if the range of rotations suggested by

542 different structures is ≥30°, i.e. equivalent to the cumulative effect of possible errors listed

543 above. For those core sections where more than one matching structure was identified, the

544 rotation that was applied was derived from the average of that required for each match. If one

545 of the matched structures was more prominent, then the applied rotation was biased towards

546 that structure.

547

548 **Appendix B: DFDP-1B core rotation validity**

549 Based on the criteria presented in Appendix A, of the 40 core sections from DFDP-1B in

550 which there was suitable quality of unrolled CT and BHTV images to attempt reorientation

551 (Figure 3), 31 were reoriented (Table S1). Prior to reorientation, fractures in these sections

552 exhibit no clustering (Figure A1a), however, a weak one does develop after reorientation

553 (Figure 5a). Since fractures in nature typically exhibit non-random orientations, this is

554 evidence that the reorientation of the CT scans was successful (Kulander et al., 1990; Paulsen

555 et al., 2002). In addition, fractures within some individual core sections (Figure A1b), and

556 fractures rotated based on a high degree of confidence (Figure A1c) contain a wide range of

557 orientations.

558

559 The recognition of fractures in unrolled CT images that are not observed in BHTV can be

560 readily explained by the higher resolution of the CT images. However, structures are also

561 observed in the BHTV logs, but not interpreted as fractures in the CT images (Figure 4). This

562   may represent noise in the BHTV images, or in the case of foliation-parallel structures, the

563   ultramylonitic foliation itself since it can be difficult to differentiate these structures. The

564   subordinate north-dipping set of fractures in the BHTV images (Figure 5b) is not recognised

565   in the orientations gathered from CT images (Figure 5a). A similar north dipping fracture set

566   was also recognised in DFDP-2B BHTV images (Massiot 2017), and their causation and

567   relevance is the focus of ongoing work.

568   **Competing Interests**

569   Authors declare that they have no conflict of interest.

570   **References**

571   Adam, L., Toy, V. and Boulton, C.: Mylonites as shales? Experimental observations of P-

572   wave anisotropy dependence on mineralogy, layering and scale, in SEG Technical Program

573   Expanded Abstracts 2016, pp. 3169–3173, Society of Exploration Geophysicists., 2016.

574   Allen, M. J., Tatham, D., Faulkner, D. R., Mariani, E. and Boulton, C.: Permeability and

575   seismic velocity and their anisotropy across the Alpine Fault, New Zealand: An insight from

576   laboratory measurements on core from the Deep Fault Drilling Project phase 1 (DFDP-1), J.

577   Geophys. Res. Solid Earth, 122(8), 6160–6179, doi:10.1002/2017JB014355, 2017.

578   Ampuero, J. P. and Mao, X.: Upper limit on damage zone thickness controlled by

579   seismogenic depth, Fault Zo. Dyn. Process. Evol. Fault Prop. Dur. Seism. Rupture, 227, 243,

580   2017.

581   Andrews, D. J.: Rupture dynamics with energy loss outside the slip zone, J. Geophys. Res.

582   Solid Earth, 110(1), 1–14, doi:10.1029/2004JB003191, 2005.

583   Barth, N. C., Toy, V. G., Langridge, R. M. and Norris, R. J.: Scale dependence of oblique

584   plate-boundary partitioning: New insights from LiDAR, central Alpine fault, New Zealand,

585   Lithosphere, 4(5), 435–448, doi:10.1130/L201.1, 2012.

586   Barth, N. C., Boulton, C., Carpenter, B. M., Batt, G. E. and Toy, V. G.: Slip localization on

587   the southern Alpine Fault New Zealand, Tectonics, 32(3), 620–640, doi:10.1002/tect.20041,

588   2013.

589   Ben-Zion, Y. and Sammis, C. G.: Characterization of Fault Zones, Pure Appl. Geophys.,

590   160(3), 677–715, doi:10.1007/PL00012554, 2003.

591   Berg, S. S. and Skar, T.: Controls on damage zone asymmetry of a normal fault zone:

592   Outcrop analyses of a segment of the Moab fault, SE Utah, J. Struct. Geol., 27(10), 1803–

593   1822, doi:10.1016/j.jsg.2005.04.012, 2005.

594   Bistacchi, A., Massironi, M. and Menegon, L.: Three-dimensional characterization of a

595   crustal-scale fault zone: The Pusteria and Sprechenstein fault system (Eastern Alps), J. Struct.

596   Geol., 32(12), 2022–2041, doi:10.1016/j.jsg.2010.06.003, 2010.

597   Bistacchi, A., Massironi, M., Menegon, L., Bolognesi, F. and Donghi, V.: On the nucleation

598   of non-Andersonian faults along phyllosilicate-rich mylonite belts, Geol. Soc. London, Spec.

599   Publ., 367(1), 185–199, doi:10.1144/sp367.13, 2012.

600   Boese, C. M. M., Townend, J., Smith, E. and Stern, T.: Microseismicity and stress in the

601   vicinity of the Alpine Fault, central Southern Alps, New Zealand, J. Geophys. Res. Solid

602   Earth, 117(2), doi:10.1029/2011JB008460, 2012.

603   Boulton, C., Yao, L., Faulkner, D. R., Townend, J., Toy, V. G., Sutherland, R., Ma, S. and

604   Shimamoto, T.: High-velocity frictional properties of Alpine Fault rocks: Mechanical data,

605   microstructural analysis, and implications for rupture propagation, J. Struct. Geol., 97, 71–92,

606   doi:10.1016/j.jsg.2017.02.003, 2017.

607   Boulton, C. J., Carpenter, B. M., Toy, V. and Marone, C.: Physical properties of surface

608   outcrop cataclastic fault rocks, Alpine Fault, New Zealand, Geochemistry, Geophys.

609   Geosystems, 13(1), doi:10.1029/2011GC003872, 2012.

610   Caine, J. S., Evans, J. P. and Forster, C. B.: Fault zone architecture and permeability structure,

611   Geology, 24(11), 1025–1028, 1996.

612 Chamberlain, C. J., Boese, C. M. and Townend, J.: Cross-correlation-based detection and

613 characterisation of microseismicity adjacent to the locked, late-interseismic Alpine Fault,

614 South Westland, New Zealand, Earth Planet. Sci. Lett., 457, 63–72,

615 doi:10.1016/j.epsl.2016.09.061, 2017.

616 Chester, F. M. and Chester, J. S.: Stress and deformation along wavy frictional faults, J.

617 Geophys. Res., 105(B10), 23421, doi:10.1029/2000JB900241, 2000.

618 Chester, F. M. and Logan, J. M.: Implications for mechanical properties of brittle faults from

619 observations of the Punchbowl fault zone, California, Pure Appl. Geophys. PAGEOPH,

620 124(1–2), 79–106, doi:10.1007/BF00875720, 1986.

621 Chester, F. M., Evans, J. P. and Biegel, R. L.: Internal structure and weakening mechanisms

622 of the San Andreas Fault, J. Geophys. Res., 98(B1), 771, doi:10.1029/92JB01866, 1993.

623 Chester, J. S. and Fletcher, R. C.: Stress distribution and failure in anisotropic rock near a

624 bend on a weak fault, J. Geophys. Res. Earth, 102(B1), 693–708, doi:10.1029/96JB02791,

625 1997.

626 Choi, J. H., Edwards, P., Ko, K. and Kim, Y. S.: Definition and classification of fault damage

627 zones: A review and a new methodological approach, Earth-Science Rev., 152, 70–87,

628 doi:10.1016/j.earscirev.2015.11.006, 2016.

629 Christensen, N. I. and Okaya, D. A.: Compressional and shear wave velocities in South

630 Island, New Zealand rocks and their application to the interpretation of seismological models

631 of the New Zealand crust, A Cont. Plate Bound. Tectonics South Island, New Zeal., 123–155,

632 2007.

633 Columbus, J., Sirguey, P. and Tenzer, R.: A free, fully assessed 15-m DEM for New Zealand,

634 Surv. Q., 66(66), 16–19, 2011.

635 Cooper, A. F. and Norris, R. J.: Anatomy, structural evolution, and slip rate of a plate-

636 boundary thrust: the Alpine Fault at Gaunt Creek, Westland, New Zealand, Geol. Soc. Am.

637 Bull., 106(5), 627–633, doi:10.1130/0016-7606(1994)106<0627:ASEASR>2.3.CO;2, 1994.

638   Cooper, A. F. and Norris, R. J.: Inverted metamorphic sequences in Alpine fault mylonites

639   produced by oblique shear within a plate boundary fault zone, New Zealand., 2011.

640   Cowie, P. A. and Scholz, C. H.: Physical Explanation for the Displacement Length

641   Relationship of Faults Using a Post-Yield Fracture-Mechanics Model, J. Struct. Geol., 14(10),

642   1133–1148, doi:10.1016/0191-8141(92)90065-5, 1992.

643   Cox, S. C., Menzies, C. D., Sutherland, R., Denys, P. H., Chamberlain, C. and Teagle, D. A.

644   H.: Changes in hot spring temperature and hydrogeology of the Alpine Fault hanging wall,

645   New Zealand, induced by distal South Island earthquakes, Geofluids, 15(1–2), 216–239,

646   2015.

647   DeMets, C., Gordon, R. G., Argus, D. F. and Stein, S.: Effect of recent revisions to the

648   geomagnetic reversal time scale on estimate of current plate motions, Geophys. Res. Lett.,

649   21(20), 2191–2194, doi:10.1029/94GL02118, 1994.

650   Donath, F. A.: Experimental study of shear failure in anisotropic rocks, Geol. Soc. Am. Bull.,

651   72(6), 985–989, doi:10.1130/0016-7606(1961)72[985:ESOSFI]2.0.CO;2, 1961.

652   Eberhart-Phillips, D., Stanley, W. D., Rodriguez, B. D. and Lutter, W. J.: Surface seismic and

653   electrical methods to detect fluids related to faulting, J. Geophys. Res., 100(B7), 12919–

654   12936, doi:10.1029/94JB03256, 1995.

655   Eberhart-Phillips, D.: Examination of seismicity in the central Alpine fault region, South

656   Island, New Zealand, New Zeal. J. Geol. Geophys., 38(4), 571–578, 1995.

657   Eccles, J. D., Gulley, A. K., Malin, P. E., Boese, C. M., Townend, J. and Sutherland, R.: Fault

658   Zone Guided Wave generation on the locked, late interseismic Alpine Fault, New Zealand,

659   Geophys. Res. Lett., 42(14), 5736–5743, doi:10.1002/2015GL064208, 2015.

660   Ellsworth, W. L. and Malin, P. E.: Deep rock damage in the San Andreas Fault revealed by P-

661   and S-type fault-zone-guided waves, Fagereng, A., Toy, V.G., Rowland, J. (Eds), Geol.

662   Earthq. Source A Vol. Honor Rick Sibson, Geol. Soc. London, Spec. Publ., 359(1), 39–53,

663   doi:10.1144/SP359.3, 2011.

664   Engelder, T.: Loading paths to joint propagation during a tectonic cycle: an example from the

665   Appalachian Plateau, U.S.A., J. Struct. Geol., 7(3–4), 459–476, doi:10.1016/0191-

666   8141(85)90049-5, 1985.

667   Faulkner, D. R., Jackson, C. A. L., Lunn, R. J., Schlische, R. W., Shipton, Z. K., Wibberley,

668   C. A. J. and Withjack, M. O.: A review of recent developments concerning the structure,

669   mechanics and fluid flow properties of fault zones, J. Struct. Geol., 32(11), 1557–1575,

670   doi:10.1016/j.jsg.2010.06.009, 2010.

671   Faulkner, D. R., Mitchell, T. M., Jensen, E. and Cembrano, J.: Scaling of fault damage zones

672   with displacement and the implications for fault growth processes, J. Geophys. Res. Solid

673   Earth, 116(5), doi:10.1029/2010JB007788, 2011.

674   Finzi, Y., Hearn, E. H., Ben-Zion, Y. and Lyakhovsky, V.: Structural properties and

675   deformation patterns of evolving strike-slip faults: Numerical simulations incorporating

676   damage rheology, Pure Appl. Geophys., 166(10–11), 1537–1573, doi:10.1007/s00024-009-

677   0522-1, 2009.

678   Geotech Consulting Limited: Amethyst Hydro Scheme Drilling Investigation Summary

679   Report., 2006.

680   Haggas, S., Brewer, T. S., Harvey, P. K. and Iturrino, G. I.: Relocating and orientating cores

681   by the integration of electrical and optical images, J. Geol. Soc. London, 158, 615–623,

682   doi:10.1144/jgs.158.4.615, 2001.

683   Ikari, M. J., Carpenter, B. M., Kopf, A. J. and Marone, C.: Frictional strength, rate-

684   dependence, and healing in DFDP-1 borehole samples from the Alpine Fault, New Zealand,

685   Tectonophysics, 630(C), 1–8, doi:10.1016/j.tecto.2014.05.005, 2014.

686   Jarrard, R. D., Paulsen, T. S. and Wilson, T. J.: Orientation of CRP-3 core, Victoria Land

687   Basin, Antarctica, Terra Antarct., 8(3), 161–166, 2001.

688   Kim, Y. S. and Sanderson, D. J.: Fault propagation, displacement and damage zones, Struct.

689   Geol. New Res., 1, 99–117, 2008.

690   Kim, Y. S., Peacock, D. C. P. and Sanderson, D. J.: Fault damage zones, J. Struct. Geol.,

691   26(3), 503–517, doi:10.1016/j.jsg.2003.08.002, 2004.

692   Kulander, B. R., Dean, S. L. and Ward, B. J.: Fracture core analysis: interpretation, logging

693   and use of natural and induced fractures in core, American Association of Petroleum

694   Geologists., 1990.

695   Langridge, R. M., Ries, W. F., Farrier, T., Barth, N. C., Khajavi, N. and De Pascale, G. P.:

696   Developing sub 5-m LiDAR DEMs for forested sections of the Alpine and Hope faults, South

697   Island, New Zealand: Implications for structural interpretations, J. Struct. Geol., 64, 53–66,

698   doi:10.1016/j.jsg.2013.11.007, 2014.

699   Lees, J. M.: RFOC: Graphics for spherical distributions and earthquake focal mechanisms. R

700   package version 3.3-3. http://CRAN.R-project.org/package=RFOC, R Packag. version, 3(2),

701   2014.

702   Li, Y. G., De Pascale, G. P., Quigley, M. C. and Gravley, D. M.: Fault damage zones of the

703   M7.1 Darfield and M6.3 Christchurch earthquakes characterized by fault-zone trapped waves,

704   Tectonophysics, 618, 79–101, doi:10.1016/j.tecto.2014.01.029, 2014.

705   Little, T. A., Cox, S., Vry, J. K. and Batt, G.: Variations in exhumation level and uplift rate

706   along the obliqu-slip Alpine fault, central Southern Alps, New Zealand, Geol. Soc. Am. Bull.,

707   117(5), 707, doi:10.1130/B25500.1, 2005.

708   Lund Snee, J. E., Toy, V. G. and Gessner, K.: Significance of brittle deformation in the

709   footwall of the Alpine Fault, New Zealand: Smithy Creek Fault zone, J. Struct. Geol., 64, 79–

710   98, doi:10.1016/j.jsg.2013.06.002, 2014.

711   Ma, S.: Distinct asymmetry in rupture-induced inelastic strain across dipping faults: An off-

712   fault yielding model, Geophys. Res. Lett., 36(20), doi:10.1029/2009GL040666, 2009.

713   Manning, C. E. and Ingebritsen, S. E.: Permeability of the continental crust: Implications of

714   geothermal data and metamorphic systems, Rev. Geophys., 37(1), 127–150,

715   doi:10.1029/1998RG900002, 1999.

716   Massiot, C.: Fracture system characterisation and implications for fluid flow in volcanic and

717   metamorphic rocks, , 1–191, 2017.

718   Massiot, C., Mcnamara, D. D. and Lewis, B.: Geothermics Processing and analysis of high

719   temperature geothermal acoustic borehole image logs in the Taupo Volcanic Zone , New

720   Zealand, Geothermics, 53, 190–201, doi:10.1016/j.geothermics.2014.05.010, 2015.

721   Massironi, M., Bistacchi, A. and Menegon, L.: Misoriented faults in exhumed metamorphic

722   complexes: Rule or exception?, Earth Planet. Sci. Lett., 307(1–2), 233–239,

723   doi:10.1016/j.epsl.2011.04.041, 2011.

724   Mauldon, M., Dunne, W. M. and Rohrbaugh, M. B.: Circular scanlines and circular windows:

725   New tools for characterizing the geometry of fracture traces, J. Struct. Geol., 23(2–3), 247–

726   258, doi:10.1016/S0191-8141(00)00094-8, 2001.

727   McNamara, D.: Exploring New Zealand's subsurface using borehole images, in Presented at

728   the 2015 New Zealand Geosciences Conference, Wellington, 25-27th November (2015).,

729   2015.

730   Mills, S. and Williams, J. N.: Generating circumferential images of tomographic drill-core

731   scans, GFZ Data Serv., doi:http://doi.org/10.5880/ICDP.5052.005, 2017.

732   Misra, S., Ellis, S. and Mandal, N.: Fault damage zones in mechanically layered rocks: The

733   effects of planar anisotropy, J. Geophys. Res. B Solid Earth, 120(8), 5432–5452,

734   doi:10.1002/2014JB011780, 2015.

735   Mitchell, T. M. and Faulkner, D. R.: The nature and origin of off-fault damage surrounding

736   strike-slip fault zones with a wide range of displacements: A field study from the Atacama

737   fault system, northern Chile, J. Struct. Geol., 31(8), 802–816, doi:10.1016/j.jsg.2009.05.002,

738   2009.

739   Mitchell, T. M. and Toy, V. G.: Photograph of the month, J. Struct. Geol., 61, 143,

740   doi:10.1016/j.jsg.2014.01.004, 2014.

741 Muir-Wood, R. and King, G. C. P.: Hydrological signatures of earthquake strain, J. Geophys.

742 Res., 98(B12), 22035, doi:10.1029/93JB02219, 1993.

743 Nasseri, M. H. B., Rao, K. S. and Ramamurthy, T.: Anisotropic strength and deformation

744 behavior of Himalayan schists, Int. J. Rock Mech. Min. Sci., 40(1), 3–23, doi:10.1016/S1365-

745 1609(02)00103-X, 2003.

746 Norris, R. J. and Cooper, A. F.: Origin of small-scale segmentation and transpressional

747 thrusting along the Alpine Fault, New Zealand, Geol. Soc. Am. Bull., 107(2), 231–240,

748 doi:10.1130/0016-7606(1995)107<0231:OOSSSA>2.3.CO;2, 1995.

749 Norris, R. J. and Cooper, A. F.: Erosional control on the structural evolution of a

750 transpressional thrust complex on the Alpine fault, New Zealand, J. Struct. Geol., 19(10),

751 1323–1342, doi:10.1016/S0191-8141(97)00036-9, 1997.

752 Norris, R. J. and Cooper, A. F.: Late Quaternary slip rates and slip-partitioning on the Alpine

753 Fault, New Zealand, J. Struct. Geol., 23(2000), 507–520, 2001.

754 Norris, R. J. and Cooper, A. F.: Very high strains recorded in mylonites along the Alpine

755 Fault, New Zealand: implications for the deep structure of plate boundary faults, J. Struct.

756 Geol., 25(12), 2141–2157, 2003.

757 Norris, R. J. and Cooper, A. F.: The Alpine Fault, New Zealand: Surface Geology and Field

758 Relationships, in A Continental Plate Boundary: Tectonics at South Island, New Zealand,

759 edited by D. Okaya, T. A. Stern, and F. Davey, pp. 157–175, American Geophysical Union.,

760 2007.

761 Norris, R. J. and Toy, V. G.: Continental transforms: A view from the Alpine Fault, J. Struct.

762 Geol., 64, 3–31, doi:10.1016/j.jsg.2014.03.003, 2014.

763 O'Brien, G. A., Cox, S. C. and Townend, J.: Spatially and temporally systematic hydrologic

764 changes within large geoengineered landslides, Cromwell Gorge, New Zealand, induced by

765 multiple regional earthquakes, J. Geophys. Res. Solid Earth, 121(12), 8750–8773, 2016.

766   Paterson, M. S. and Wong, T. F.: Experimental rock deformation - The brittle field, Springer-

767   Verlag Berlin Heidelberg., 2005.

768   Paulsen, T. S., Jarrard, R. D. and Wilson, T. J.: A simple method for orienting drill core by

769   correlating features in whole-core scans and oriented borehole-wall imagery, J. Struct. Geol.,

770   24(8), 1233–1238, doi:10.1016/S0191-8141(01)00133-X, 2002.

771   Peacock, D. C. P. and Sanderson, D. J.: Effects of layering and anisotropy on fault geometry,

772   J. Geol. Soc. London., 149(5), 793–802, doi:10.1144/gsjgs.149.5.0793, 1992.

773   Price, N. J.: Mechanics of jointing in rocks, Geol. Mag., 96(2), 149–167,

774   doi:10.1017/S0016756800060040, 1959.

775   Priest, S.: Discontinuity Analysis for Rock Engineering, Springer Science & Business Media.,

776   1993.

777   Rattenbury, M. and Isaac, M.: The QMAP 1:250 000 Geological Map of New Zealand

778   project, New Zeal. J. Geol. Geophys., 8306(April), doi:10.1080/00288306.2012.725417,

779   2012.

780   Reed, J. J.: Mylonites, cataclasites, and associated rocks along the Alpine fault, South Island,

781   New Zealand, New Zeal. J. Geol. Geophys., 7(4), 645–684,

782   doi:10.1080/00288306.1964.10428124, 1964.

783   Rice, J. R., Sammis, C. G. and Parsons, R.: Off-fault secondary failure induced by a dynamic

784   slip pulse, Bull. Seismol. Soc. Am., 95(1), 109–134, doi:10.1785/0120030166, 2005.

785   Savage, E.: Investigating Rock Mass Conditions and Implications for Tunnelling and

786   Construction of the Amethyst Hydro Project, Harihari, University of Canterbury., 2013.

787   Savage, H. M. and Brodsky, E. E.: Collateral damage: Evolution with displacement of

788   fracture distribution and secondary fault strands in fault damage zones, J. Geophys. Res. Solid

789   Earth, 116(3), doi:10.1029/2010JB007665, 2011.

790   Savage, H. M., Keranen, K. M., Schaff, D. and Dieck, C.: Possible Precursory Signals in

791   Damage Zone Foreshocks, Geophys. Res. Lett., 2017.

792   Schulz, S. E. and Evans, J. P.: Mesoscopic structure of the Punchbowl Fault, Southern

793   California and the geologic and geophysical structure of active strike-slip faults, J. Struct.

794   Geol., 22(7), 913–930, doi:10.1016/S0191-8141(00)00019-5, 2000.

795   Shigematsu, N., Otsubo, M., Fujimoto, K. and Tanaka, N.: Orienting drill core using

796   borehole-wall image correlation analysis, J. Struct. Geol., 67(PB), 293–299,

797   doi:10.1016/j.jsg.2014.01.016, 2014.

798   Sibson, R. H.: Earthquake faulting as a structural process, J. Struct. Geol., 11(1–2), 1–14,

799   doi:10.1016/0191-8141(89)90032-1, 1989.

800   Sibson, R. H., White, S. H. and Atkinson, B. K.: Structure and distribution of fault rocks in

801   the Alpine Fault Zone, New Zealand, Geol. Soc. London, Spec. Publ., 9(1), 197–210, 1981.

802   Simpson, G. D. H., Cooper, A. F. and Norris, R. J.: Late Quaternary evolution of the Alpine

803   Fault Zone at Paringa, South Westland, New Zealand, New Zeal. J. Geol. Geophys., 37(1),

804   49–58, doi:10.1080/00288306.1994.9514600, 1994.

805   Stanley, C. R. and Hooper, J. J.: POND: An Excel spreadsheet to obtain structural attitudes of

806   planes from oriented drillcore, Comput. Geosci., 29(4), 531–537, doi:10.1016/S0098-

807   3004(03)00033-5, 2003.

808   Stern, T., Okaya, D., Kleffmann, S., Scherwath, M., Henrys, S. and Davey, F.: Geophysical

809   exploration and dynamics of the Alpine Fault Zone, A Cont. Plate Bound. Tectonics South

810   Island, New Zeal. Geophys. Monogr. Ser. 175, 207–233, doi:10.1029/175GM11, 2007.

811   Sutherland, R., Eberhart-Phillips, D., Harris, R. A., Stern, T., Beavan, J., Ellis, S., Henrys, S.,

812   Cox, S., Norris, R. J., Berryman, K. R., Townend, J., Bannister, S., Pettinga, J., Leitner, B.,

813   Wallace, L., Little, T. A., Cooper, A. F., Yetton, M. and Stirling, M.: Do Great Earthquakes

814   Occur on the Alpine Fault in Central South Island, New Zealand?, in A Continental Plate

815   Boundary: Tectonics at South Island, New Zealand, vol. 175, edited by D. Okaya, Stern, T.,

816   and F. Davey, pp. 235–251, American Geophysical Union., 2007.

817   Sutherland, R., Toy, V. G., Townend, J., Cox, S. C., Eccles, J. D., Faulkner, D. R., Prior, D.

818   J., Norris, R. J., Mariani, E., Boulton, C., Carpenter, B. M., Menzies, C. D., Little, T. A.,

819   Hasting, M., De Pascale, G. P., Langridge, R. M., Scott, H. R., Reid Lindroos, Z., Fleming, B.

820   and Kopf, J.: Drilling reveals fluid control on architecture and rupture of the Alpine fault,

821   New Zealand, Geology, 40(12), 1143–1146, doi:10.1130/G33614.1, 2012.

822   Sutherland, R., Townend, J., Toy, V. G., Upton, P., Coussens, J. and DFDP2, S. T.: Extreme

823   hydrothermal conditions at an active plate-bounding fault, Nature, 546, 137–140,

824   doi:10.1038/nature22355, 2017.

825   Sylvester, A. G.: Strike-Slip Faults, Geol. Soc. Am. Bull., 100(November), 1666–1703,

826   doi:10.1130/0016-7606(1988)100<1666:SSF>2.3.CO;2, 1988.

827   Templeton, E. L., Rice, J. R., Viesca, R. C., Templeton, E. L. and Rice, J. R.: Off-fault

828   plasticity and earthquake rupture dynamics: 2. Effects of fluid saturation, J. Geophys. Res.

829   Solid Earth, 113(9), doi:10.1029/2007JB005530, 2008.

830   Terzaghi, R. D.: Sources of Error in Joint Surveys, Géotechnique, 15(3), 287–304,

831   doi:10.1680/geot.1965.15.3.287, 1965.

832   Tippett, J. M. and Kamp, P. J. J.: Quantitative relationships between uplift and relief

833   parameters for the Southern Alps, New Zealand, as determined by fission track analysis,

834   Earth Surf. Process. Landforms, 20(2), 153–175, 1995.

835   Townend, J. and Zoback, M. D.: How faulting keeps the crust strong, Geology, 28(5), 399–

836   402, doi:10.1130/0091-7613(2000)28<399:HFKTCS>2.0.CO, 2000.

837   Townend, J., Sutherland, R., Toy, V. G., Eccles, J. D., Boulton, C., Cox, S. C. and

838   McNamara, D.: Late-interseismic state of a continental plate-bounding fault: Petrophysical

839   results from DFDP-1 wireline logging and core analysis, Alpine Fault, New Zealand,

840   Geochemistry, Geophys. Geosystems, 14(9), 3801–3820, doi:10.1002/ggge.20236, 2013.

841   Townend, J., Sutherland, R., Toy, V. G., Doan, M. L., Célérier, B., Massiot, C., Coussens, J.,

842   Jeppson, T., Janku-Capova, L., Remaud, L., Upton, P., Schmitt, D. R., Pezard, P., Williams,

843 J., Allen, M. J., Baratin, L. M., Barth, N., Becroft, L., Boese, C. M., Boulton, C., Broderick,

844 N., Carpenter, B., Chamberlain, C. J., Cooper, A., Coutts, A., Cox, S. C., Craw, L., Eccles, J.

845 D., Faulkner, D., Grieve, J., Grochowski, J., Gulley, A., Hartog, A., Henry, G., Howarth, J.,

846 Jacobs, K., Kato, N., Keys, S., Kirilova, M., Kometani, Y., Langridge, R., Lin, W., Little, T.,

847 Lukacs, A., Mallyon, D., Mariani, E., Mathewson, L., Melosh, B., Menzies, C., Moore, J.,

848 Morales, L., Mori, H., Niemeijer, A., Nishikawa, O., Nitsch, O., Paris, J., Prior, D. J., Sauer,

849 K., Savage, M. K., Schleicher, A., Shigematsu, N., Taylor-Offord, S., Teagle, D., Tobin, H.,

850 Valdez, R., Weaver, K., Wiersberg, T. and Zimmer, M.: Petrophysical, Geochemical, and

851 Hydrological Evidence for Extensive Fracture-Mediated Fluid and Heat Transport in the

852 Alpine Fault's Hanging-Wall Damage Zone, Geochemistry, Geophys. Geosystems, 18(12),

853 4709–4732, doi:10.1002/2017GC007202, 2017.

854 Toy, V.: Rheology of the Alpine Fault mylonite zone: deformation processes at and below the

855 base of the seismogenic zone in a major plate boundary structure, University of Otago., 2008.

856 Toy, V. G., Prior, D. J. and Norris, R. J.: Quartz fabrics in the Alpine Fault mylonites:

857 Influence of pre-existing preferred orientations on fabric development during progressive

858 uplift, J. Struct. Geol., 30(5), 602–621, doi:10.1016/j.jsg.2008.01.001, 2008.

859 Toy, V. G., Craw, D., Cooper, A. F. and Norris, R. J.: Thermal regime in the central Alpine

860 Fault zone, New Zealand: Constraints from microstructures, biotite chemistry and fluid

861 inclusion data, Tectonophysics, 485(1–4), 178–192, doi:10.1016/j.tecto.2009.12.013, 2010.

862 Toy, V. G., Boulton, C. J., Sutherland, R., Townend, J., Norris, R. J., Little, T. A., Prior, D. J.,

863 Mariani, E., Faulkner, D., Menzies, C. D., Scott, H. and Carpenter, B. M.: Fault rock

864 lithologies and architecture of the central Alpine fault, New Zealand, revealed by DFDP-1

865 drilling, Lithosphere, 7(2), 155–173, doi:10.1130/l395.1, 2015.

866 Toy, V. G., Sutherland, R., Townend, J., Allen, M. J., Becroft, L., Boles, A., Boulton, C.,

867 Carpenter, B., Cooper, A., Cox, S. C., Daube, C., Faulkner, D. R., Halfpenny, A., Kato, N.,

868 Keys, S., Kirilova, M., Kometani, Y., Little, T., Mariani, E., Melosh, B., Menzies, C. D.,

869   Morales, L., Morgan, C., Mori, H., Niemeijer, A., Norris, R., Prior, D., Sauer, K., Schleicher,

870   A. M., Shigematsu, N., Teagle, D. A. H., Tobin, H., Valdez, R., Williams, J., Yeo, S., Baratin,

871   L. M., Barth, N., Benson, A., Boese, C., Célérier, B., Chamberlain, C. J., Conze, R.,

872   Coussens, J., Craw, L., Doan, M. L., Eccles, J., Grieve, J., Grochowski, J., Gulley, A.,

873   Howarth, J., Jacobs, K., Janku-Capova, L., Jeppson, T., Langridge, R., Mallyon, D., Marx, R.,

874   Massiot, C., Mathewson, L., Moore, J., Nishikawa, O., Pooley, B., Pyne, A., Savage, M. K.,

875   Schmitt, D., Taylor-Offord, S., Upton, P., Weaver, K. C., Wiersberg, T. and Zimmer, M.:

876   Bedrock geology of DFDP-2B, central Alpine Fault, New Zealand, New Zeal. J. Geol.

877   Geophys., 60(4), 497–518, doi:10.1080/00288306.2017.1375533, 2017.

878   Turnbull, I. M., Mortimer, N. and Craw, D.: Textural zones in the Haast Schist—a

879   reappraisal, New Zeal. J. Geol. Geophys., 44(1), 171–183,

880   doi:10.1080/00288306.2001.9514933, 2001.

881   Upton, P., Song, B. R. and Koons, P. O.: Topographic control on shallow fault structure and

882   strain partitioning near Whataroa, New Zealand demonstrates weak Alpine Fault, New Zeal.

883   J. Geol. Geophys., 1–8, doi:10.1080/00288306.2017.1397706, 2017.

884   Vermilye, J. M. and Scholz, C. H.: The process zone: A microstructural view of fault growth,

885   J. Geophys. Res. Earth, 103(B6), 12223–12237, doi:10.1029/98JB00957, 1998.

886   Warr, L. N. and Cox, S.: Clay mineral transformations and weakening mechanisms along the

887   Alpine Fault, New Zealand, in Geological Society, London, Special Publications, vol. 186,

888   edited by R. E. Holdsworth, R. A. Strachan, J. F. Magloughlin, and R. J. Knipe, pp. 85–101,

889   The Geological Society, London., 2001.

890   Wellman, H.: Data for the Study of Recent and Late Pleistocene Faulting in the South, New

891   Zeal. J. Sci. Technol., 34(4), 270–288, 1953.

892   Williams, J. N., Toy, V. G., Massiot, C., McNamara, D. D. and Wang, T.: Damaged beyond

893   repair? Characterising the damage zone of a fault late in its interseismic cycle, the Alpine

894   Fault, New Zealand, J. Struct. Geol., 90, 76–94, doi:10.1016/j.jsg.2016.07.006, 2016.

895   Williams, J. N., Toy, V. G., Smith, S. A. F. and Boulton, C.: Fracturing, fluid-rock interaction

896   and mineralisation during the seismic cycle along the Alpine Fault, J. Struct. Geol., 103, 151–

897   166, doi:https://doi.org/10.1016/j.jsg.2017.09.011, 2017a.

898   Williams, J. N., Toy, V. G., Massiot, C. and McNamara, D.: X-ray Computed Tomography

899   and borehole televiewer images of the Alpine Fault's hanging-wall, New Zealand: Deep Fault

900   Drilling Project phase 1 (DFDP-1) and Amethyst Hydro Project (AHP), GFZ Data Serv.,

901   doi:http://doi.org/10.5880/ICDP.5052.004, 2017b.

902   Wilson, J. E., Chester, J. S. and Chester, F. M.: Microfracture analysis of fault growth and

903   wear processes, Punchbowl Fault, San Andreas system, California, J. Struct. Geol., 25(11),

904   1855–1873, doi:10.1016/S0191-8141(03)00036-1, 2003.

905   Wright, C. A.: Geology and paleoseismicity of the central Alpine Fault, New Zealand., 1998.

906   Yukutake, Y., Ito, H., Honda, R., Harada, M., Tanada, T. and Yoshida, A.: Fluid-induced

907   swarm earthquake sequence revealed by precisely determined hypocenters and focal

908   mechanisms in the 2009 activity at Hakone volcano, Japan, J. Geophys. Res. Solid Earth,

909   116(4), doi:10.1029/2010JB008036, 2011.

910   Zangerl, C., Loew, S. and Eberhardt, E.: Structure, geometry and formation of brittle

911   discontinuities in anisotropic crystalline rocks of the central Gotthard massif, Switzerland,

912   Eclogae Geol. Helv., 99(2), 271–290, doi:10.1007/s00015-006-1190-0, 2006.

913

916
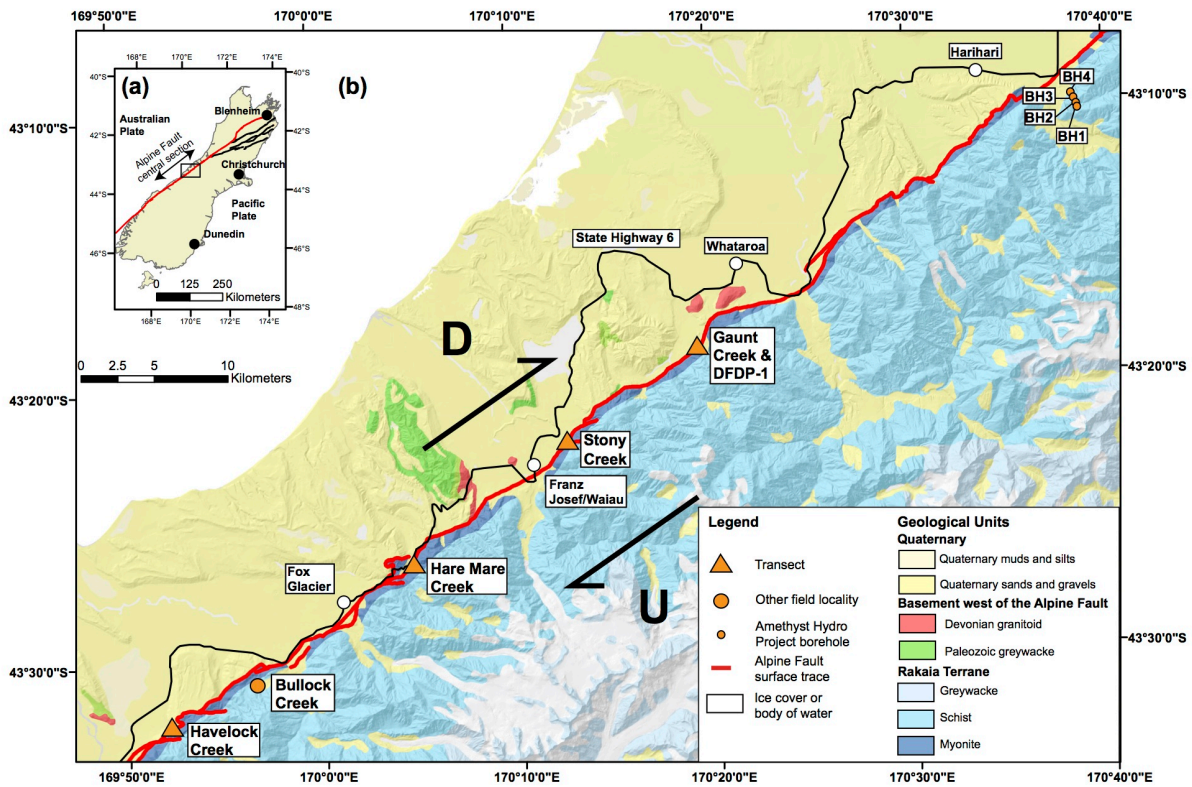
Figure 1: (a) Location map for Alpine Fault (red line) and Marlborough Faults (black line) in the

South Island of New Zealand. Box shows extent of (b), a location map for the DFDP-1 and AHP

boreholes, and field transects. The generalised underlying geology is derived from the GNS Science

1:250000 QMAP project (Rattenbury and Isaac, 2012) and has been draped over a digital elevation

model (Columbus et al., 2011).

922

923 **Figure 2**
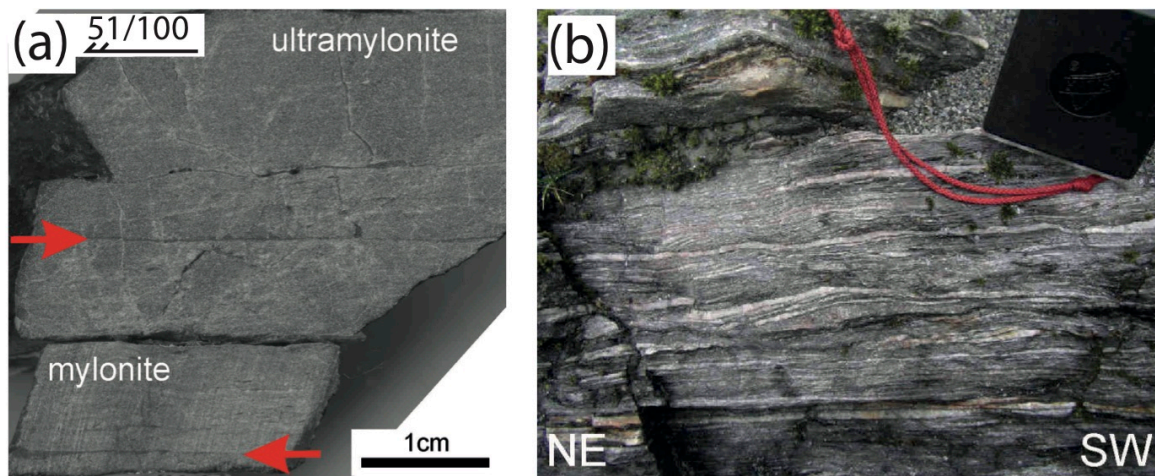
924

925 Figure 2: (a) Quartzofeldspathic Alpine Fault ultramylonite that gradually grades to mylonite at the

926 base of the image. A foliation defined by alternating white quartzofeldspathic bands and dark grey

927 mica bands is hard to distinguish in the ultramylonite but is more apparent in the mylonite. (b) The

928 well foliated Alpine Fault protomylonite-mylonite transition. Compass is 5 cm wide. Both images

929 previously presented in Toy, (2008). The sample in (a) was taken from Gaunt Creek, as was the photo

930 in (b).

931

932   **Figure 3**
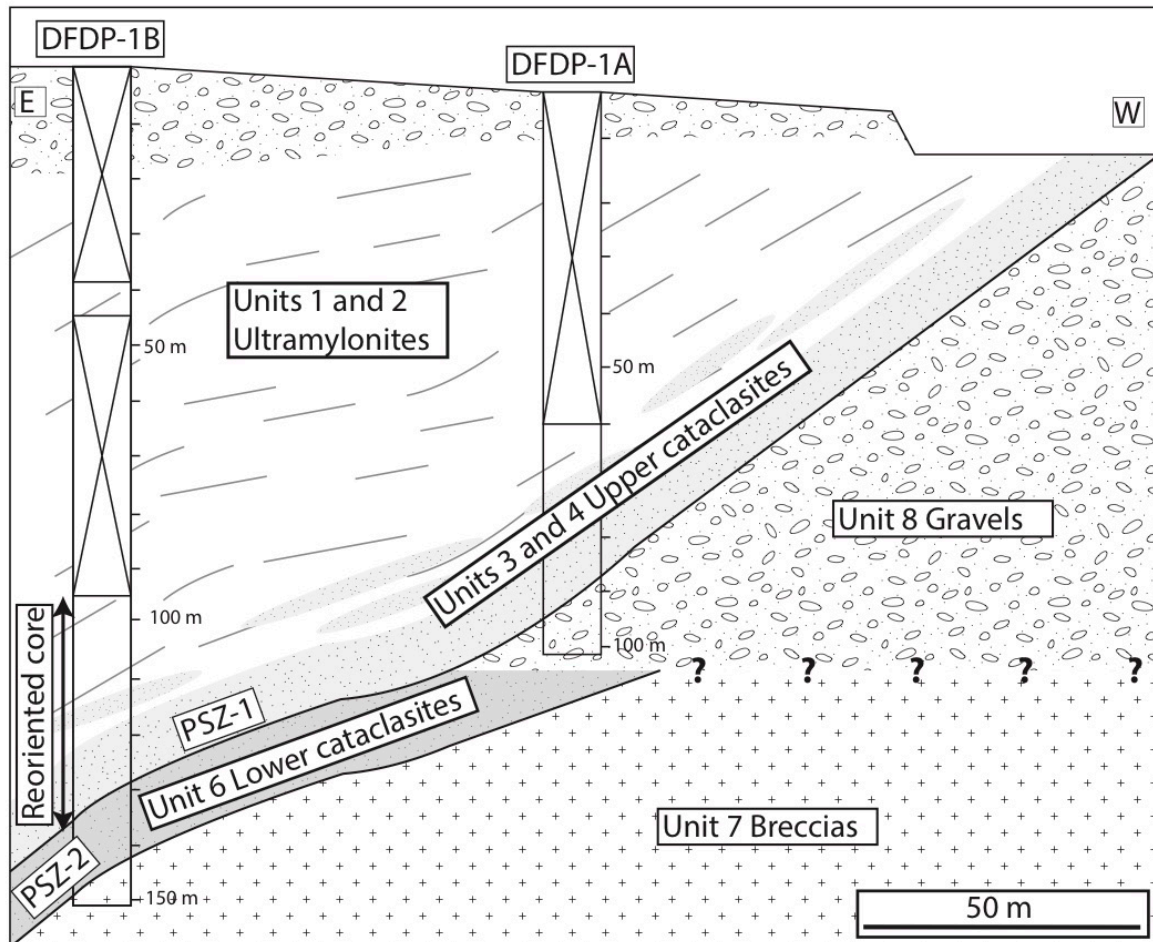
933

934   Figure 3: Cross section through the DFDP-1 boreholes, showing interval where reoriented drill-core is

935   located. Boxes with diagonal lines depict intervals in borehole with no core recovery, grey lines

936   represent mylonitic foliation. Modified from Sutherland et al., (2012), with lithological units

937   previously defined by Toy et al., (2015).

938
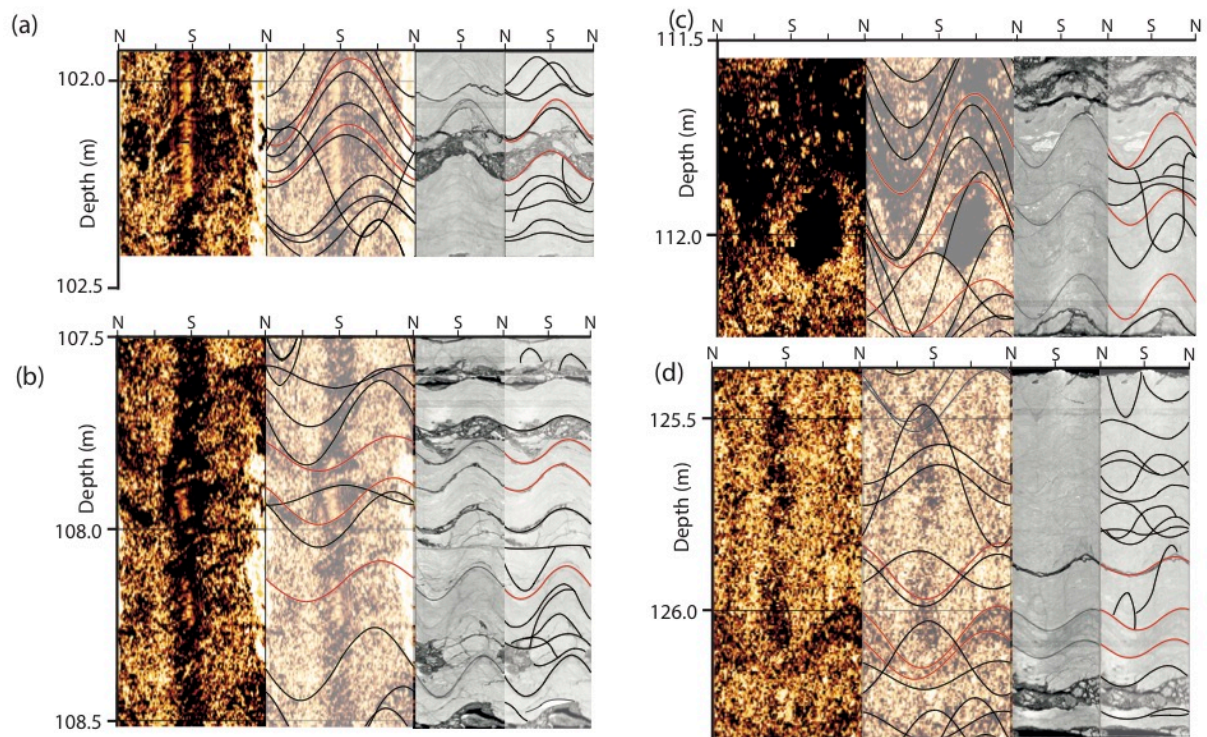
Figure 4

Figure 4: Examples of matching structures between BHTV images and unrolled CT images. In each image, the first two columns are the BHTV amplitude image, without and with interpretations respectively, whilst the third and fourth columns depict the unrolled CT image over the same interval, also without and with interpretations. Fractures that have been traced in red indicate those that were matched to reorientate core.

947 **Figure 5**
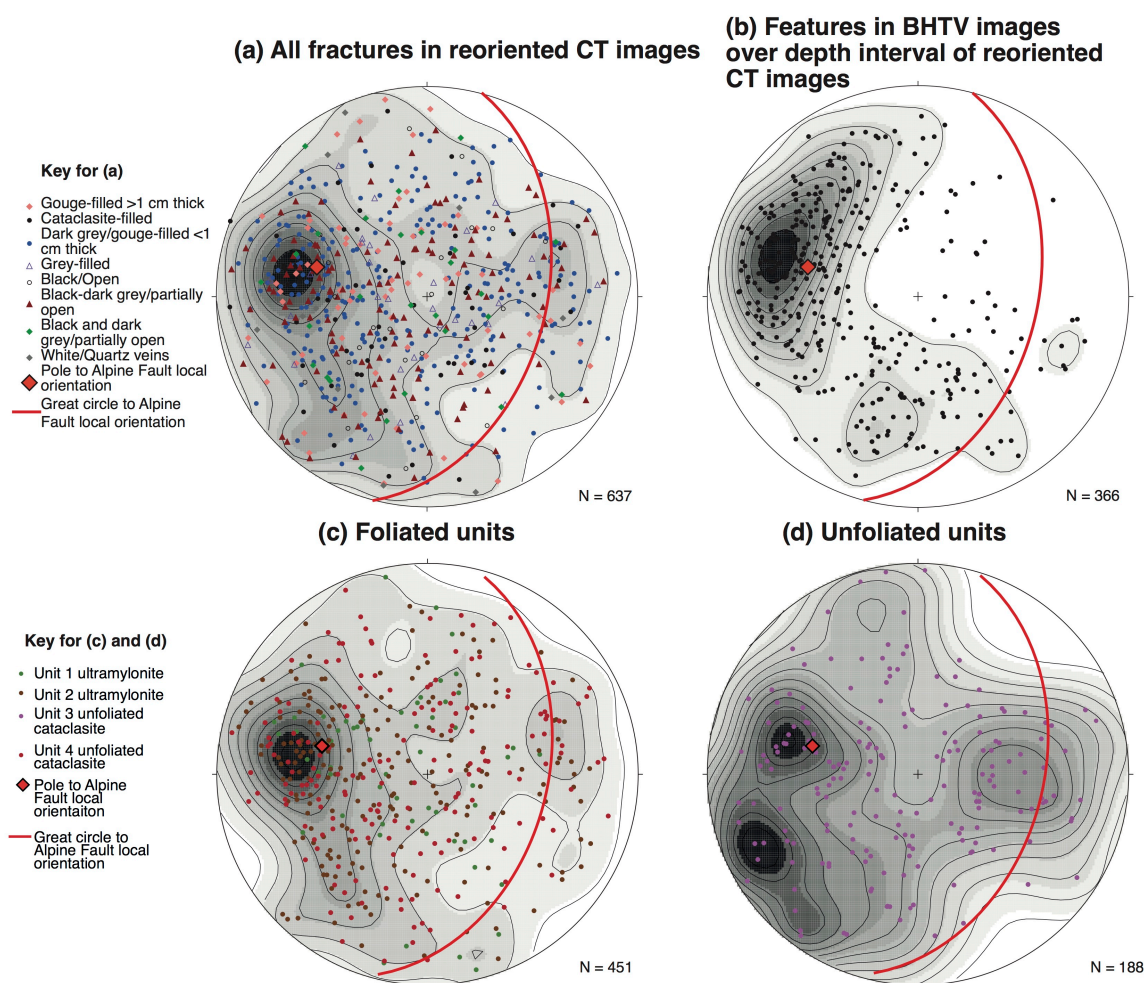
Figure 5: Lower hemisphere equal area stereoplots depicting orientation of fractures in DFDP-1.
Contouring on stereoplots was applied to poles that are weighted depending on their orientation
correction w (see Sect. 3.2), and that are rounded to the nearest whole number. Contours were then
generated for the weighted poles using a probability distribution calculated by a Kernel function in the
RFOC package for R (Lees, 2014). Great circle represents orientation of Alpine Fault plane and
foliation at DFDP-1 site (Townend et al., 2013). (a) Orientation of all fractures that were reoriented by
matching structures between unrolled CT images and BHTV images, sorted by fracture type (Williams
et al., 2016). (b) Orientation of features recognised in the BHTV images over the interval of reoriented
core (94-126 m in DFDP-1B). Fracture orientations extracted from reoriented DFDP-1 CT images in
(c) foliated units and (d) unfoliated units, using the DFDP-1 lithological classification scheme (Toy et
al., 2015).

960 **Figure 6**

(a) (b) (c)

CT Number Key: 500 2250 4000
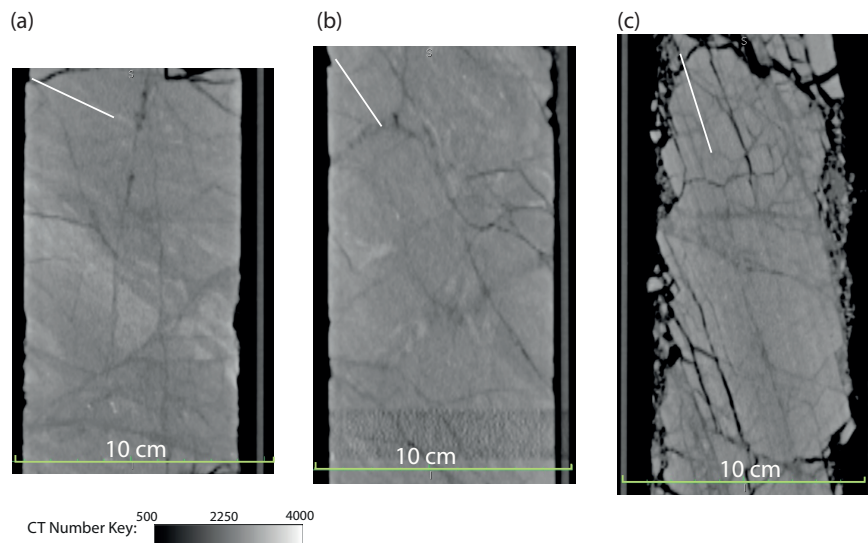
961

962 Figure 6: The relationship between foliation and fracture orientations in Alpine Fault ultramylonite, as

963 observed in 2D CT image slices of DFDP-1 drill-core. Intervals are (borehole, core section and run,

964 depth interval): (a) DFDP-1A 55-1 75.45-75.62 m, (b) DFDP-1B 35-1 102.49-102.64 m, and (c)

965 DFDP-1B 25-2, 44.80-45.20 m. In (a) and (b) fractures tend to cross-cut the ultramylonitic foliation

966 (orientation represented by white line in top left corner of each image). (c) Fractures show a greater

967 preference to be aligned parallel to the foliation. Note that (c) was previously shown in Williams et al.,

968 (2016), and is not included in the reorientation analysis in Figure 5, as there was no BHTV imagery

969 for this interval.
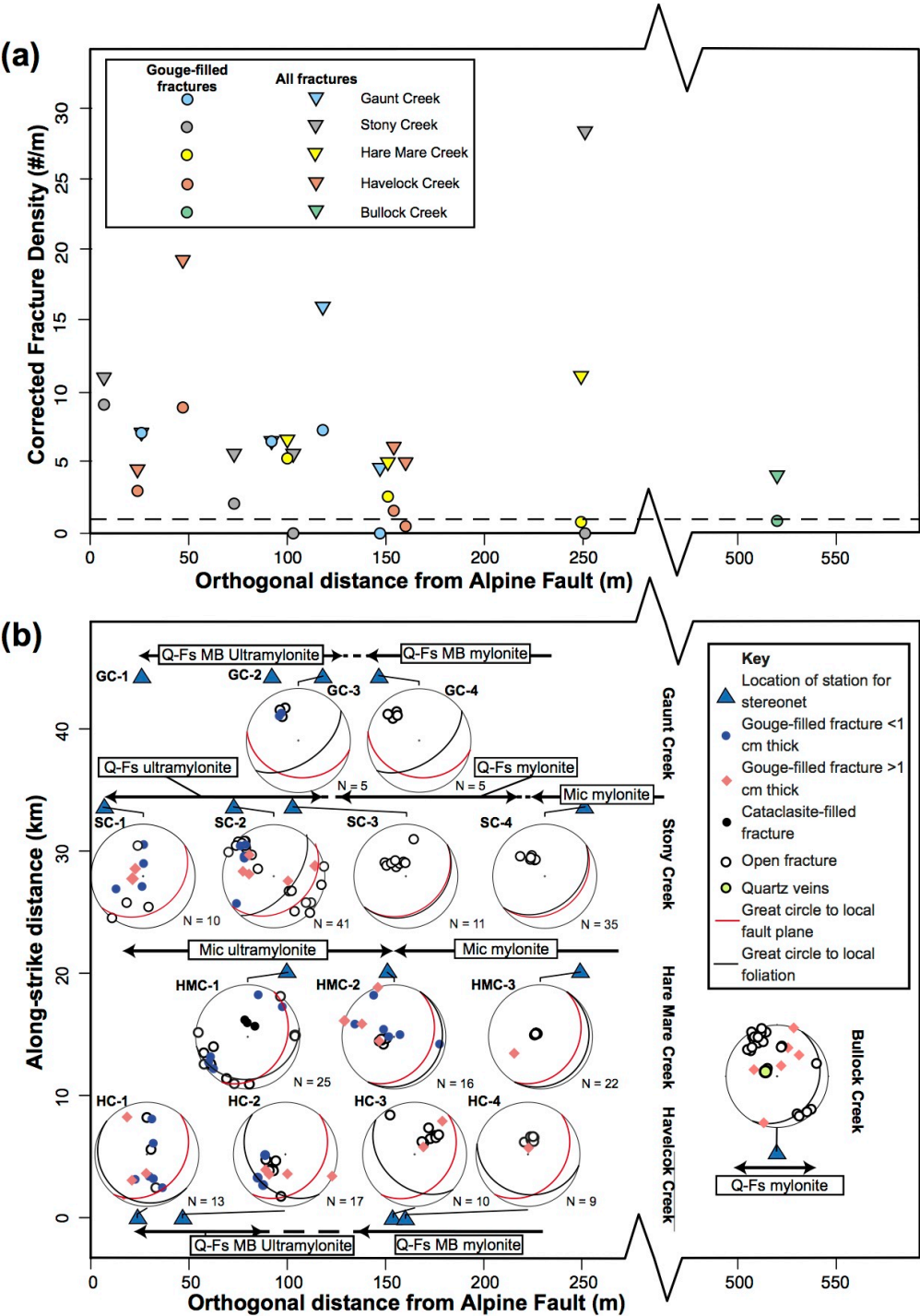
Figure 7

Figure 7: (a) Corrected fracture density at all stations for gouge-filled fractures and all fractures.

Dashed line indicates a corrected fracture density of 1 fracture/metre. No orientation data was

collected at Gaunt Creek stations 1 and 2, so fracture density is calculated from the two perpendicular

transects. (b) Compilation of stereoplots for fracture orientations at each field station. Stations have

976   been plotted as a function of distance from the fault and distance along-strike (with respect to

977   Havelock Creek) along within fault rock lithologies. Dashed lines indicate gradational or obscured

978   lithological boundaries. Qfs, Quartzofeldspath; MB, metabasic; Mic, Micaceous. For field cross

979   sections and location of stations, see Figure S1. Results are also summarised in Table S2.

980 **Figure 8**
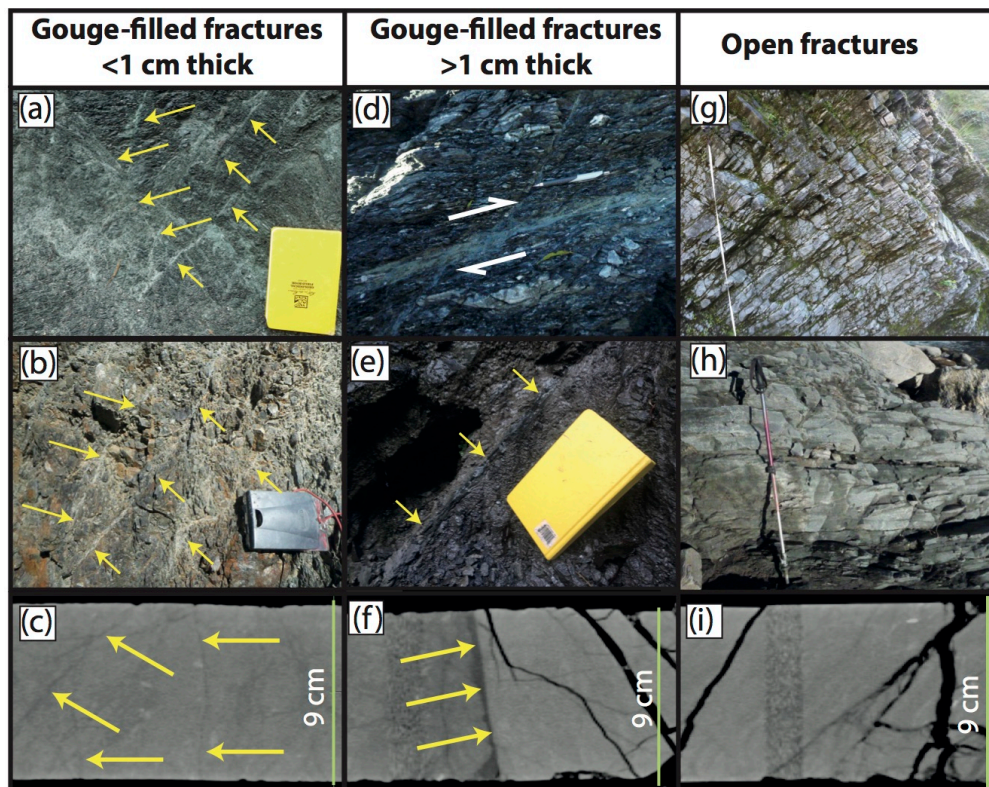
981

982 Figure 8: Examples of the three main types of fractures observed in the field around the Alpine Fault,

983 and correlative fractures in DFDP-1 CT scans. (a-c) Thin gouge-filled fractures (yellow arrows) have a

984 range of orientations and found exclusively within 160 m from the fault. They are equivalent to type

985 iii of fractures from Williams et al., (2016). (d-f) Thicker gouge and cataclasite filled fractures are

986 equivalent to type i and ii fractures of Williams et al. (2016) and may be observed at all distances from

987 the Alpine Fault. Offset markers can be observed across these fractures (e.g. the vein indicated by the

988 pen and white arrows in (d)). (g-i) Open fractures are mainly foliation-parallel. Equivalent to type v

989 fractures of Williams et al., (2016). Location of field photos: (a) Waikukupa thrust, (b) and (g) Stony

990 Creek, (d) and (h) Havelock Creek, (e) Bullock Creek. Compass clinometer 8 cm and yellow notebook

991 20 cm in length. Measuring tape in (e) 1.1 m long, walking pole in (g) 1 m in length. DFDP-1 CT scan

992 intervals: (c) DFDP-1B 56-2 125.35-125.49 m, (f) DFDP-1B 35-1 102.00-102.15 m, (i) DFDP-1B 33-

993 2 99.45-99.60 m
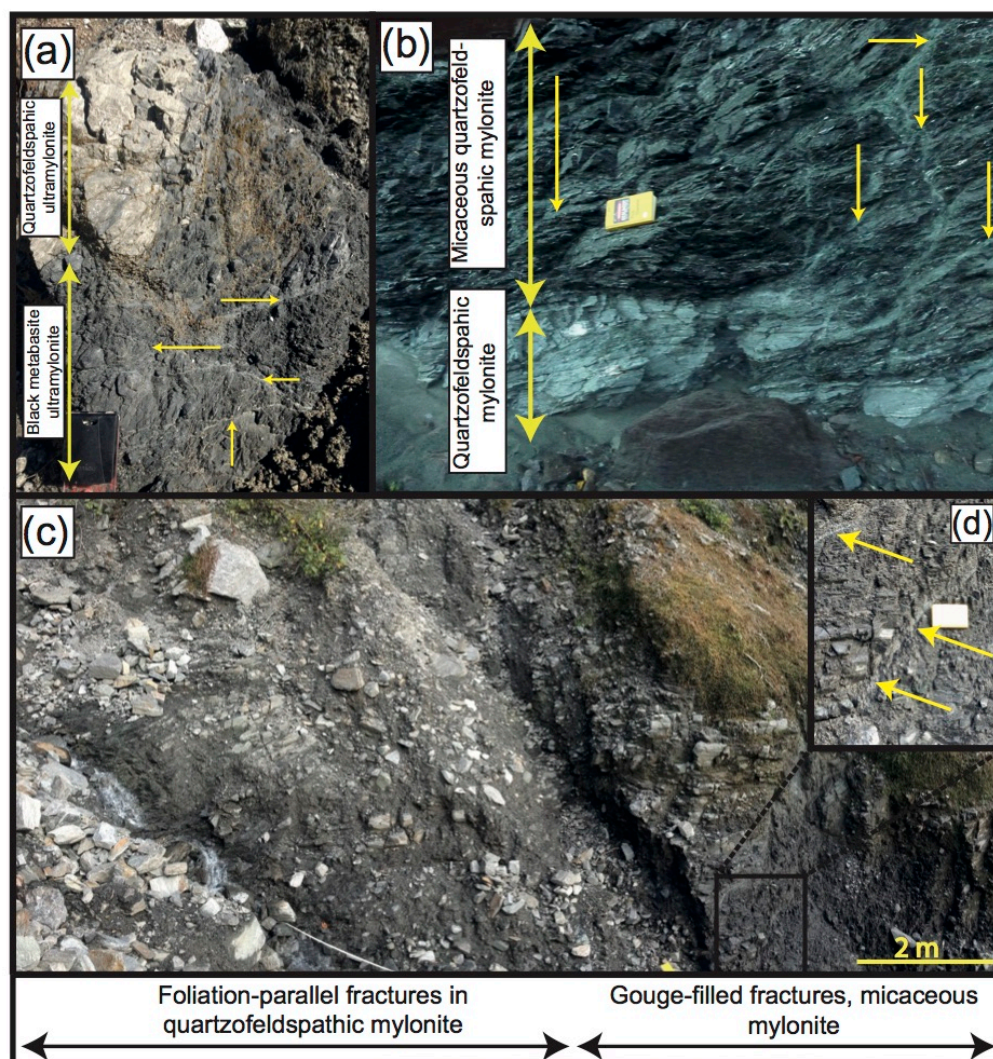
Figure 9

Figure 9: Field observations of changes in fracture density at lithological contacts. (a&b) Intervals of

micaceous and metabasite mylonite containing a relatively high proportion of gouge filled fractures

(denoted by yellow arrows) compared to interlayered quartzofeldspathic mylonite. (c) Transition from

micaceous mylonite to quartzofeldspathic mylonite coincides with furthest extent of intensive gouge-

filled fractures, as shown by yellow arrows in (d). Taken at (a) Gaunt Creek, (b) Havelock Creek,

(c&d) Hare Mare Creek. Compass clinometer 8 cm and yellow notebook 20 cm in length.

1002   **Figure 10**

1003
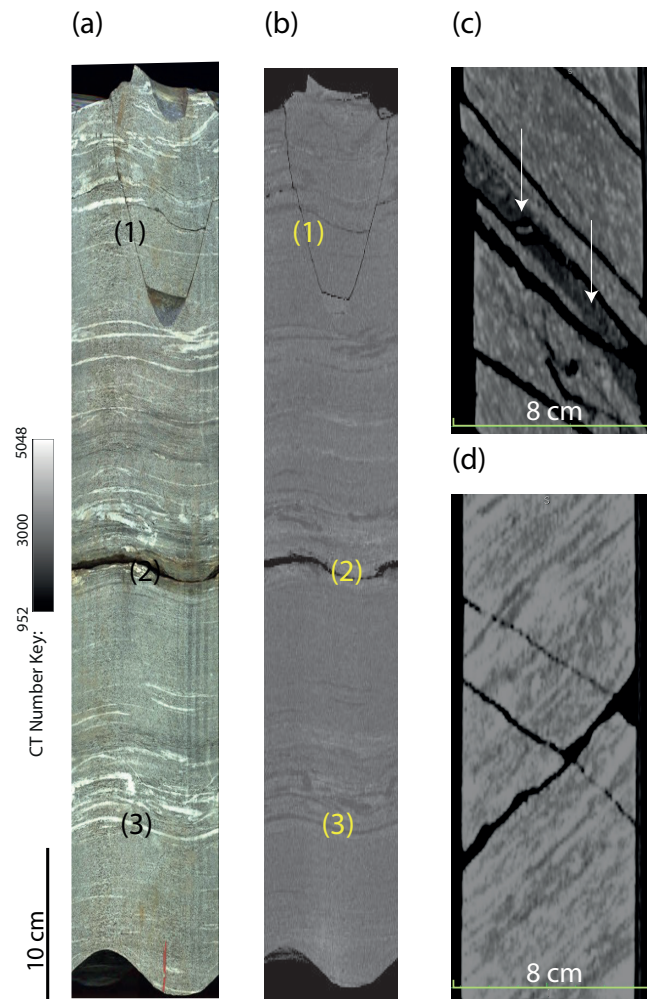
1004   Figure 10: Fractures in the Amethyst Hydro Project (AHP) drill-core. Unrolled images of AHP drill-

1005   core (BH1 45-2 124.3-124.9 m) taken by (a) DMT core scanner and (b) generated from a CT image.

1006   (1) Identifies fracture cutting across foliation, (2) foliation-parallel fracture with alteration halo, (3)

1007   foliation defined by quartzofeldspathic bands that have low CT numbers. (c&d) Core-axial parallel CT

1008   image slices of AHP drill-core. In (c) white arrows point to a 'crush zone' sub parallel to foliation

1009   (BH2 75-2 155.92-156.04 m). (d) more variable fracture orientations identified in BH4 (Section 70-4

1010   196.62-196.80 m).

1011

1012 **Figure 11**

Legend:
- BH1
- BH2
- BH3
- BH4
- Pole to regional Alpine Fault
- Pole to regional foliation
- Great circle to regional Alpine Fault
- Great circle to regional foliation

N = 239

1013
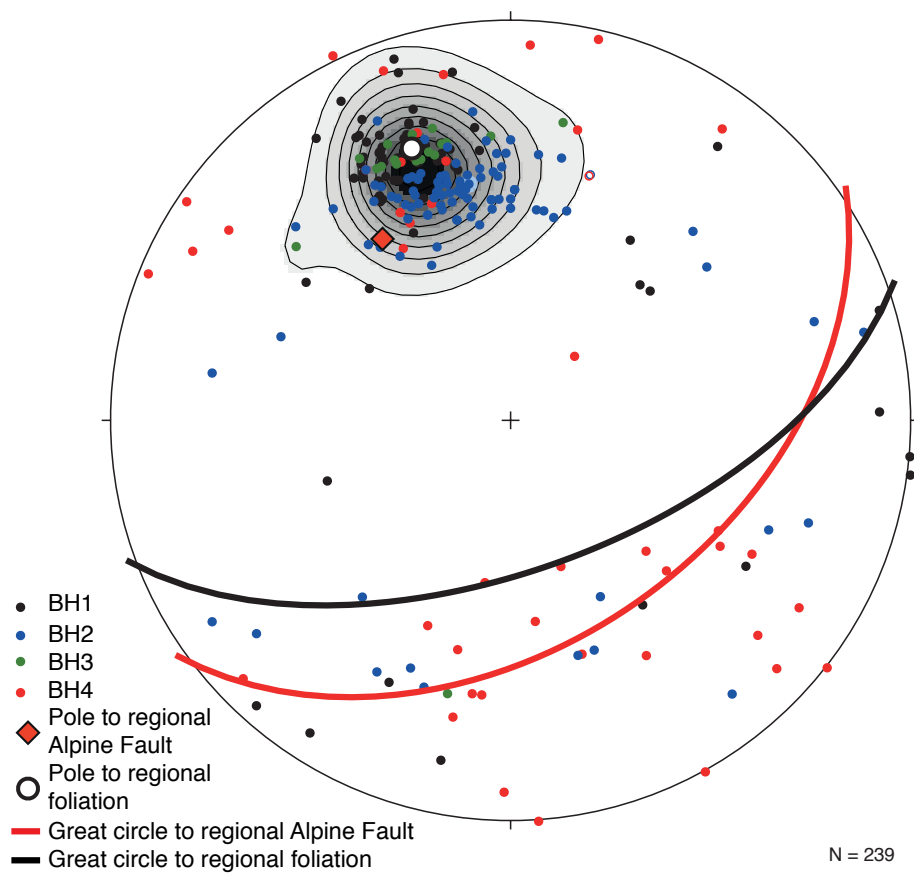
1014 Figure 11: Equal area, lower hemisphere projection of fracture orientations recognised in CT scans of

1015 AHP drill-core separated by borehole. Contours plotted with weighted poles (see Figure 5).

1016

1017 **Figure 12**

1018
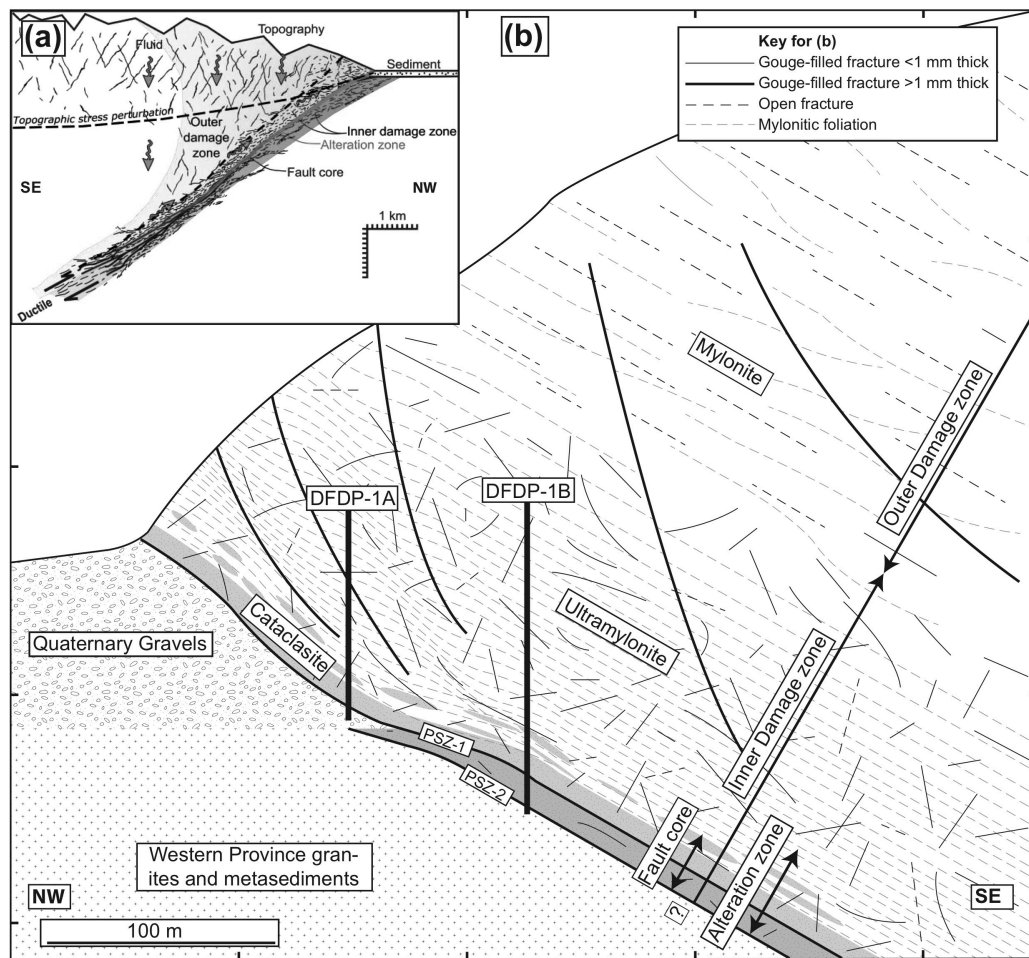
1019 Figure 12: Schematic cross sections through the Alpine Fault illustrating its hanging-wall

1020 structure. (a) Crustal-scale cross section illustrating the flower shaped geometry of the outer

1021 damage zone (after Townend et al., (2017)). (b) A thrust section within the central section of

1022 the Alpine Fault, depicting fracture network, its relationship to foliation, and the distribution

1023 of subsidiary faults. Respective position of DFDP-1 boreholes also shown. Constructed from

1024 cross sections previously presented in Norris and Cooper, (2007) and Sutherland et al.,

1025 (2012).

1026 **Figure 13**

1027
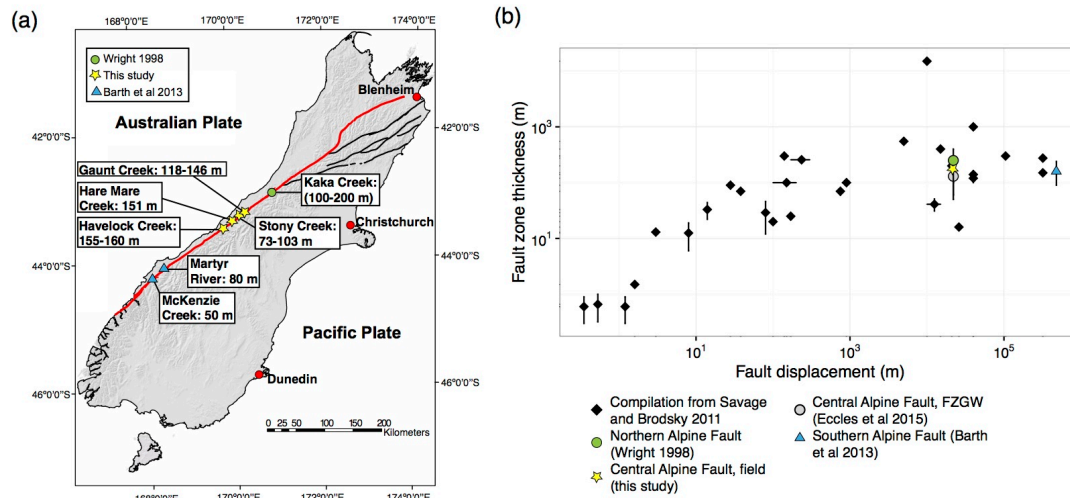
1028 Figure 13: (a) Compilation of estimates of the 'inner damage zone' width on the Pacific Plate

1029 side of the Alpine Fault (red line) from four creek sections in this study (Gaunt Creek, Stony

1030 Creek, Hare Mare Creek and Havelock Creek). This is combined with other along-strike

1031 estimates of damage zone thickness for the Pacific Plate side of the Alpine Fault: McKenzie

1032 Creek and Martyr River (Barth et al., 2013) and Kaka Creek (Wright, 1998). (b) Log-log plot

1033 of fault zone thickness as a function of fault displacement previously presented in Savage and

1034 Brodsky, (2011), combined with estimates made for the Alpine Fault assuming footwall

1035 damage is no more extensive than in the hanging-wall. Displacement for the Alpine Fault is

1036 480 km (Norris and Cooper, 2007; Wellman, 1953). However, convergence along the Alpine

1037 Fault's central section requires that it erodes its own fault rocks so these points are plotted to

1038 reflect only the brittle displacement the rocks themselves have accommodated as they are

1039 exhumed through the seismogenic zone (22 km, Barth et al., (2012)). Error bars reflect

1040 uncertainty in constraining fault zone width (as for example, footwall damage is largely

1041 unknown), not necessarily variability in fault zone thickness.

1042

1043 **Figure A1**

1044
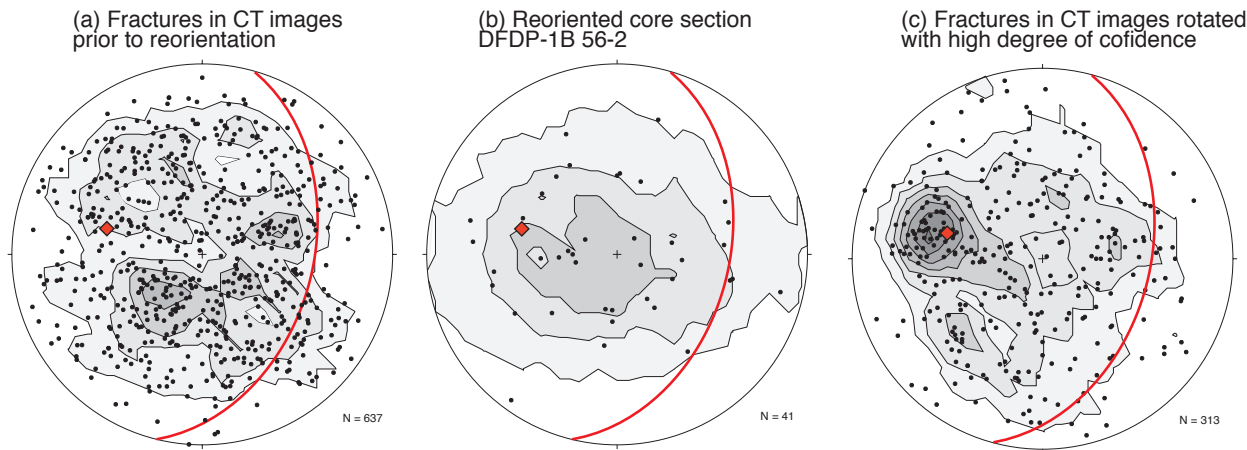
1045 Figure A1: Stereoplots to tests the confidence in reorientations applied to rotate DFDP-1 CT

1046 scan fracture orientations into geographic coordinates. Red great circle and diamond in each

1047 plot represents plane and pole to the Alpine Fault orientation measured in DFDP-1B. Plotted

1048 with Kamb contours with intervals of two standard deviations. (a) Orientation of fractures

1049 shown in Figure 5a before rotation, (b) orientation of reoriented fractures within a single core

1050 section (DFDP-1B 56-2), and (c) orientation of fractures in CT images from core sections that

1051 were oriented with a high degree of confidence with BHTV images.

1052

	Number of fractures	Resultant Plane dip direction	Resultant Plane dip	Resultant vector length (Cluster intensity, 2 s.f.)
All reoriented DFDP-1 CT fractures	637	80	58	0.58
Reoriented DFDP-1 CT fractures, foliated units	451	87	58	0.58
Reoriented DFDP-1 CT fractures, unfoliated units	188	71	61	0.58
DFDP-1B BHTV features (depth interval 94-126 m)	365	103	47	0.72
AHP Fractures	239	164	58	0.76

1055 Table 1: Clustering analysis of the different fracture datasets documented in this study, using

1056 the resultant vector methodology outlined by Priest, (1993). DFDP-1 foliated units comprise

1057 ultramylonites and foliated cataclasites (Units 1, 2 and 4 of Toy et al., (2015)). DFDP-1

1058   unfoliated units comprise unfoliated cataclasites (Unit 3 of Toy et al., (2015)). The resultant

1059   vector orientation for each dataset, which has been converted to spherical coordinates, is also

1060   reported. See text for full details.